Cryogenic Deformation of Two Comet and Asteroid Analogs Under Varying Conditions of Saturation

by

Jared William Graham Atkinson

Submitted to the Department of Earth, Atmospheric and Planetary Sciences
in partial fulfillment of the requirements for the degree of

Master of Science in Planetary Sciences

at the

MASSACHUSETTS INSTITUTE OF TECHNOLOGY

September 2016

Signature redacted

Author ... .
Department of Earth, Atmospheric and Planetary Sciences
June 6, 2016

Signature redacted

Certified by..... ...
Sara Seager
Class of 1941 Professor of Physics and Planetary Science
Thesis Supervisor

Signature redacted

Accepted by .....
Robert D. van der Hilst
Schlumberger Professor of Earth Sciences, Department Head

Cryogenic Deformation of Two Comet and Asteroid Analogs Under Varying Conditions of Saturation

by

Jared William Graham Atkinson

Submitted to the Department of Earth, Atmospheric and Planetary Sciences
on June 6, 2016, in partial fulfillment of the
requirements for the degree of
Master of Science in Planetary Sciences

Abstract

Sample retrieval from extraterrestrial bodies and in situ resource utilization (ISRU) activities have been identified as some of the most important scientific endeavors of the coming decade. With the failure of Rosetta's Philae lander to penetrate the surface of comet 67P and obtain a sample due to the high compressive strength of the surface, it is becoming obvious that knowledge of the mechanical properties of materials that might be encountered in such environments and under such conditions is critical to future mission success.

Two comet/asteroid analogs (Indiana limestone and Bishop tuff), selected based on their contrasting mechanical properties and porosities, were tested under constant displacement to failure (in most cases) at extraterrestrial conditions of cryogenic temperatures (295 K down to 77 K) and light confining pressures (1 to 5 MPa). The compressive strength of both materials was determined under varied conditions of saturation, from oven-dried (~0% water content) to fully saturated, and both brittle and ductile behavior was observed. The saturated limestone increased in strength from ~30 MPa (at 295 K) to >200 MPa (at 77 K), while the Bishop tuff increased in strength from 13 MPa at 295 K to 165 MPa at 150 K. Additional experiments demonstrated that thermal cycling reduces the compressive strength of limestone, while an increase in confining pressure from 5 MPa to 30 MPa at 200 K significantly increases the strength (from 62 MPa to 85 MPa respectively) of saturated tuff.

The results of this study will be useful to future sample retrieval missions or ISRU maneuvers. The large increase in compressive strength of these saturated materials at cryogenic temperatures means that future missions will need to prepare technology that has the energetic and mechanical capability to penetrate very hard substrates as they are likely to encounter.

Thesis Supervisor: Sara Seager
Title: Class of 1941 Professor of Physics and Planetary Science

Acknowledgments

The work presented here would not have been possible without the help of many, many individuals.

First and foremost are my advisors and mentors at MIT, Sara Seager and William Durham. Without their guidance and support, my tenure at MIT may have ended much too early. Their commitment to me and to the science has helped this study evolve into something I can be proud of.

Other MIT faculty has also been critical in supporting the work, namely Dan Cziczo and Richard Binzel, both strong sources of encouragement. Many technical and personal discussions were had with Brian Evans, Yves Bernabe, Brad Hager, Michael Fehler, Dan Brown, Dan Burns, and Anna Shaughnessy, and for those I am very thankful. Vicki McKenna and Roberta Allard, who helped me navigate the sometimes complex world of graduate administration, deserve particular acknowledgment.

The experiments in this study were performed with the integral help of David Goldsby and Chao Qi at the University of Pennsylvania, and Manika Prasad at the Colorado School of Mines. A huge amount of gratitude is owed to them for allowing me access to their labs and to their minds.

While my time at MIT certainly involved a lot of time in the office, it wasn't all work. My fellow students Frank Centinello, Gabi Melo, and Ben Corbin were a constant support. Niek Beckers and Chris Giebe, who were my Cambridge family, continue to be my family even though the miles between us have increased significantly. Another Cambridge family, my friends and colleagues at the Muddy (especially my manager Mike Grenier), deserve thanks as well for letting a Canadian work in an American pub. Thanks also to my MOG club friends Migel, Renato, Juan Esteban, Justin, and Josimar, who kept reminding me that I still had a career to return to.

There are many, many others that need to be thanked. Kris Zacny at Honeybee Robotics, Angel Abbud-Madrid and Chris Dryer at the Colorado School of Mines are just a few. The list is long, and if you shared a drink, coffee, or even a passing conversation with me during the past few years, your contribution to my time at MIT is greatly appreciated, and your name belongs on this list.

Beyond the MIT community, I thank my mother, father, and sister for always supporting

me through every crazy, unpredictable decision I make. They have always let me know that, success or failure, family will always be there for you.

And finally my wife, without whom none of this would be possible. Her constant and unconditional support made all the difference. Thank you, from the bottom of my heart.

Contents

List of Figures

List of Tables

Chapter 1

Introduction

The National Research Council identified sample retrieval from extraterrestrial bodies as one of the most important scientific endeavors of the next decade [1]. Major advancements in our understanding of the initial stages, conditions, and processes of the formation of our solar system, as well as the nature of the interstellar materials that were incorporated into it, will be made with the return of pristine, cryogenically-preserved surface and subsurface samples of various primitive solar system bodies.

The most primordial bodies in the solar system — asteroids, comets, Kuiper Belt Objects (KBOs), and objects in the Oort cloud (OCOs) — are all remnants of its early period, containing intact material from the collapse of the local molecular cloud and the onset of solar system formation [1]. Chondrites are especially valuable as the least processed of these bodies, containing preserved pre-solar grains whose compositions reflect processes in ancient stars and supernovae, while KBOs and OCOs retain pristine records of the initial solar nebula chemistry.

Direct sampling of these bodies, at various depths, will greatly contribute to our understanding of the primordial solar system, its initial composition and formation, as well as the variety of changes that it has endured since its earliest beginnings. Of particular interest is the presence of extraterrestrial water-ice.

Ice has recently become a focus for in-situ resource utilization (ISRU) [2, 3]. Water, in the form of ice, is a necessity for sustainable human development off-planet and for processing of extraterrestrial ore. Additionally, water (frozen within soils and rocks) is identified as one of the most likely substrates in which to find evidence of extraterrestrial life [4]. As most

of the water in our solar system is locked up as ice [5], detailed analysis of how to extract, drill, or otherwise attain access to this resource is critical.

In addition to ISRU, the behavior of water-saturated material is important in all aspects of our current space programs; from landing of spacecraft on potentially frozen surfaces, to collection of subsurface samples and anchoring mechanisms [6, 7], to planetary defense tactics where it is necessary to understand how a projectile impacting an asteroid/comet will alter its course [8].

With the recent successful landing of the spacecraft Philae on the comet 67P — and its reported difficulties [9, 10, 11] — it is becoming clear that a detailed understanding of the mechanical properties of the surface of any extraterrestrial body of interest is necessary.

Recent work identified potential issues with extraterrestrial drilling and extraction [4, 12, 13], and focused on the energy requirement for drilling into permanently frozen extraterrestrial soils. However, little is currently known about the behavior of water-saturated consolidated or semi-consolidated rocks at extreme low temperatures as one may encounter in our solar system [5, 14]. Limited laboratory work [15, 16, 17, 18] shows conflicting results, often due to the inherent difficulty in performing experiments at such extreme temperatures. In this study, we used a unique cryogenic tri-axial apparatus at MIT [19] to observe the behavior of two analogs — Indiana limestone and Bishop tuff — at low temperatures, with specific focus on the dependence of compressive strength on sub-freezing temperature.

The results of the experiments show that the presence of ice in the pore spaces of an extraterrestrial analog can significantly increase its overall strength at cold temperatures. As many of the current space exploration targets involve ice-bearing bodies [1, 7], this has profound implications.

Chapter 1 of this study provides a more detailed background of the scientific advancements that can be made with an advancement in drilling and sampling techniques, the location and form of ice in our solar system, and a discussion of failure in consolidated materials, providing the necessary knowledge for the subsequent experimental analysis. The preparation of analog samples, along with the general experimental procedures for compressive strength tests are covered in Chapter 2. Chapter 3 details the main set of experiments determining the compressive strength of both a limestone and a tuff (serving as extraterrestrial analogs), from sample preparation through to interpretation of the results. Additional experiments are also described that were run to provide insight into the failure of the analog

materials under very specific situations (that of reloading, thermal cycling, and increased confining pressure). Finally, Chapter 4 discusses the results of the experiments in the context of current and future missions, and what insights gained from this study can provide for space explorers.

1.1 Background on In Situ Sample Retrieval

The return of pristine surface and subsurface samples from celestial, primordial bodies will contribute to major advancements in our understanding of the formation of our solar system. Obtaining these samples, however, will constitute a vast challenge — logistically and technologically — for future explorers and missions.

Shallow samples (~1 m) obtained from icy bodies including asteroids, comets, KBOs and OCOs will first and foremost be a step further than has ever been achieved before, as subsurface samples at any depth have yet to be successfully acquired. This shallow material can provide direct measurements of the depth that space weathering can reach, as well as evidence of impact gardening and regolith thickness and composition.

Deeper samples (~10 m) can begin to probe the depth of the regolith layer, and whether the body is monolithic or a gravitational aggregate [20] (depending on the total radius of the body). Sampling at significant depths (~100 m), again depending on the body radius, can probe the core of small bodies, accessing potentially pristine material that remains untouched from its initial formation in the beginning of the solar system. Internal differentiation could be directly observed and measured at these depths, and the complexity in composition would mirror such complexity in the early solar system.

Assuming that such bodies are products of accretionary processes, the deeper a sample is taken the older the sampled material should be. In the presence of impacts however, only the deepest samples may access virgin material, and only if the impacts were somehow constrained to the shallower portions. Direct in situ measurements have the ability to provide insight into the impact history of such bodies (how deep the impacted material resides, what is its composition and age, and how it relates to the underlying "host" material).

Sampling will also play a key role in our search for organic matter in the solar system. Organic matter has been identified on asteroids (or comets) [21] and satellites such as Titan [22], and is speculated to exist on KBOs and potentially OCOs [1]. Analysis of cryogenically

preserved samples from these bodies could help in tracing the origins of primitive organics. The deepest samples will provide a window into the unadulterated past, while the shallow subsurface could provide evidence for organic material being easily transported and deposited from body to body.

While the bulk of our current knowledge of asteroid and comet composition comes from measurements of recovered meteorites and the (very) rare in situ collection of dust samples, the true composition and saturation is not well known. In addition to direct sampling, remote measurements can provide additional information but are not without their limitations. Typical remote sensing of planetary surfaces is done using neutron, near-infrared, and gamma ray spectrometry, along with radar measurements [23, 24, 25, 26, 27]. Neutron, near-infrared, and gamma ray spectrometry are particularly useful at identifying the presence of water as well as mineral compositions. However, they are confined to the very near-surface, from the upper microns (near-infrared) to tens of centimeters depth (neutron and gamma ray). Radar measurements, while able to penetrate to significant depths (depending on the frequency of the source), sacrifice resolution for penetration ability. Higher frequencies (required for increased resolution) attenuate quickly in most mediums. The combination of shallow and deep remote sensing measurements, however, can give an indication of the material composition and saturation of the subsurface, which can in turn aid researchers in developing and identifying appropriate analogs for experimentation on Earth.

1.2 Ice in the Solar System

Water-ice abounds in our solar system, existing on bodies as close to the sun as Mercury [24] and as far as the Oort cloud [28]. In the early solar system, the density of water molecules was high enough to condense ice from the gas phase at a temperature that defines the "snow line" [29]. Various forms of ice, due to the different crystalline forms that water can take, dominate under certain pressure and temperature regimes.

The most common form of ice on Earth is ice Ih [28]. Ice Ih and has a hexagonal crystal structure, while the cubic variant (ice Ic) exists in minute amounts in the upper atmosphere and is created through vapor deposition of ice at very low temperatures (220 K and lower) [30]. Many other phases of ice exist, and the solid-solid transition from one phase to another is accomplished under various pressure and temperature conditions not often encountered

terrestrially [31]. Throughout the solar system, ice I is expected to exist on planetary bodies and satellites in conjunction with various other phases, as well as rock and ice mixtures [32]. Additionally, amorphous ice (lacking a discernible crystal structure) is a dominant phase in the interstellar medium [33], and is typically formed from the rapid cooling of liquid water.

In general, the presence of ice, hydrated minerals, or (potentially) clathrates speaks to the heating history, impact history, and current pressure and temperature regimes of the target body. In turn, we can use this information to probe fundamental questions such as the accretion and supply of water in the early solar system, the role that bombardment may have played in transporting water throughout the solar system, whether life currently exists on other bodies today or in the past, and whether Mars or Venus hosted ancient aqueous environments and the conditions under which they evolved.

The presence of amorphous ice indicates very rapid cooling at temperatures less than 130 K [34]. Though there is still speculation as to the crystallinity of ice during the circumstellar disk and planetary formation, surviving amorphous ice from the molecular cloud collapse should be preserved outside Saturn's orbit [35]. Discovery of this ice could provide crucial information on the primordial solar system. Additionally, the ratio of amorphous to crystalline ice can say much about temperature, pressure, radiation flux, and thermal conversion regimes [35, 36].

Satellites such as Enceladus and Europa are theorized to have water oceans beneath icy crusts, and samples from these bodies (both shallow and deep) will give insight into the organic chemistry of the remote past, especially if water from below the crust is constantly being brought up to shallower depths within geysers [37].

Mars and Venus have also shown evidence of having ancient aqueous environments [1], and plans have already begun to probe the icy depths of polar craters in search of evidence of water, and of life [12]. If evidence of aqueous environments conducive to early life exists, and whether life emerged and still exists today, it may be found in the frozen regolith (and below) of the polar craters. On larger bodies such as planets, depth is directly related to time: the deeper the investigation, the farther back the observation. With increased sampling depth, the past life of Mars and Venus is open to us, with all its complexity.

All of the applications of sampling in icy environments mentioned so far are part of ambitious plans that are currently being evaluated [1, 38]. Small body targets and characterization of their surface/subsurface material has been identified as a top science priority.

However, the coming decades will bring additional challenges and opportunities.

Evidence for the presence of ice in the asteroid belt is limited to hydration signatures from infrared spectrometry, outgassing observed as comet tails, and remote measurements [29].

Ice will likely be found beneath the surface of small bodies, shielded from solar radiation and the vacuum of space, where it can persist for billions of years near the surface within what is termed the "shallowly buried snow line" [29]. Recent work has shown consistently that ice can be expected to be found near the surface not only of comets, but also of main belt asteroids and various moons [29, 39, 40, 41, 42, 43].

For ice to be found in the subsurface, a small body (i.e. asteroid) must contain sufficient porosity to have accumulated volatiles in the past. Porosity on asteroids is thought to exist in two forms: micro and macro [44]. Microporosity consists of pore spaces, pore throats, and voids between grains, on the order of tens of micrometers. Macroporosity refers to the large-scale voids and fractures on asteroids, and may be the result of its collisional history.

From measurements of bulk density and volume, asteroid porosity estimates can be obtained. The most porous asteroids appear to be C-type, with overall porosities ranging from 0% to 20% and higher [44]. It is within the porous C-type family, in particular carbonaceous chondrites, where we expect to find substantial deposits of water ice.

1.3 Failure Theory

For almost any material, the application of sufficient load (either in compression or in tension) will cause failure. The failure, however, can have different meanings in various disciplines, and is intricately tied to the microscopic and macroscopic mechanical properties of the material. In this study, failure is defined as the inability of a material to support higher stress (or load), and the maximum stress supported by the material is termed the peak stress.

As used in this study, the peak stress is synonymous with compressive strength (ultimate strength, or simply strength), and the terms are used interchangeably.

The behavior of the material under compression both before and after peak stress is reached (failure has occurred) can be broadly broken into two regimes: brittle and ductile. Transitional behavior can also occur between the two regimes, where the material exhibits

both brittle and ductile deformation characteristics. An overview of the particulars for each regime can be seen in Figure 1-1.

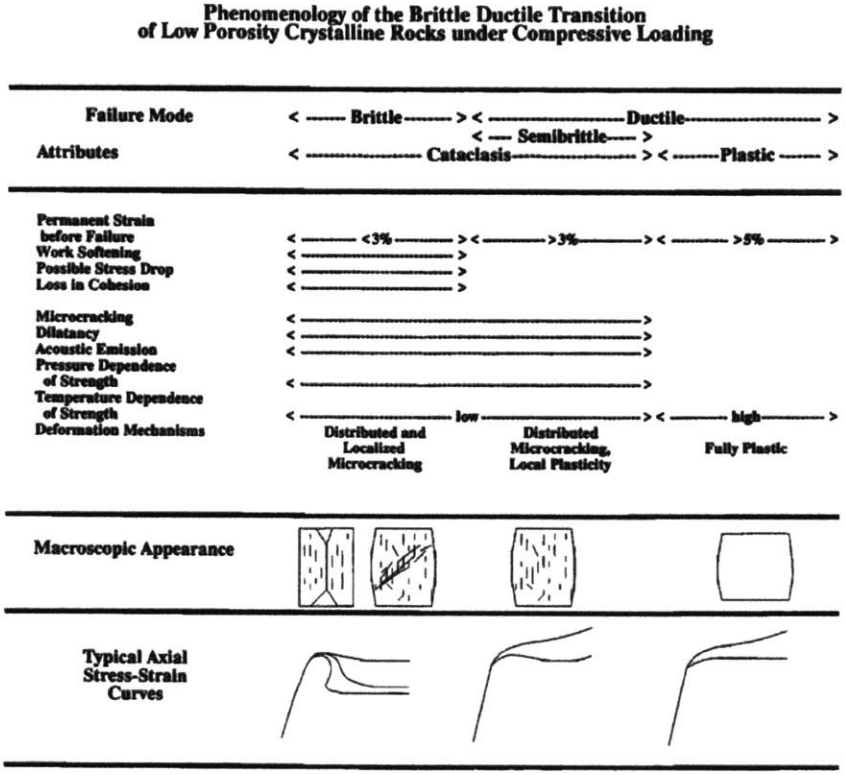

Figure 1-1: Schematic diagram illustrating the characteristics of the brittle and ductile fields, as well as the brittle-ductile transition. The shape of the stress/strain curves and microscopic appearance of the samples are important to note, as they help to indicate the failure method. From [45].

1.3.1 Brittle Failure

Brittle failure is best exemplified by standing a pencil upright on a table and pressing down on it. The length of the pencil likely will not change much (though it may bend): it will not become shorter and fatter. If the applied load is released before it breaks, it will return to its original shape; this is known as elastic behavior. If enough pressure is applied the pencil will snap in two, with a very clear (or localized) fracture plane.

Brittle failure occurs when it is not preceded by any significant amount of permanent deformation, though the behavior is not entirely elastic prior to failure [46]. A small amount of non-elastic behavior, known as yielding, often occurs just before failure. The point at

which the behavior changes from elastic to non-elastic is known as the yield stress.

Failure in the brittle field occurs when small fractures begin to form within the material, typically at pre-existing defects that are optimally oriented, and join together to form a localized plane of failure [47, 48]. This is the typical macroscopic fracture or fault seen in many failed brittle materials.

There are two principal modes of brittle failure. A shear fracture occurs when displacement is parallel to the fracture surface (generally $\sim 45^{\circ}$ from the largest principal stress), and is dominant in triaxial tests that employ high confining pressure [46]. Alternatively, at low confining stress or high differential stresses, axial splitting may occur. This involves the failure plane running parallel to the maximum principal stress and the fracture opening being parallel to the minimum principal stress [46].

The brittle field is relatively insensitive to strain rate and temperature changes, but is highly sensitive to pressure. An increase in confining pressure tends to reduce brittle deformation, as localization of the initial small cracks is inhibited, and distributed deformation is encouraged.

Brittle failure can be broken into various stages, with each stage representing specific physical mechanisms within the material. Often, a stress-strain graph is helpful in observing these stages (Figure 1-2). In the first stage, there is rapid hardening of the material as pre-existing microcracks that are oriented perpendicular to the direction of loading are closed. This is generally reversible, though some pore collapse that occurs may be irreversible.

The second stage is often known as linear-elastic behavior, and involves the elastic deformation of grains. While generally reversible, there may be some sliding on pre-existing failure planes. The rock type and amount of confining pressure will greatly affect the size of this stage, which is capped by the yield stress.

The third stage, following the onset of the yield stress, shows a departure from elasticity. Dilation may occur as microcracks proliferate and propagate (generally parallel to the load direction).

The fourth stage occurs when the microcracks coalesce and localize into a plane. Though it is not known if localization occurs before or after reaching peak stress, the material can no longer support higher stresses, and failure has been achieved. Following failure, the material may still be able to support a reduced load as the friction along the fracture plane resists the applied stress, while others may have failed so catastrophically that they can essentially

support no load (Figure 1-2).

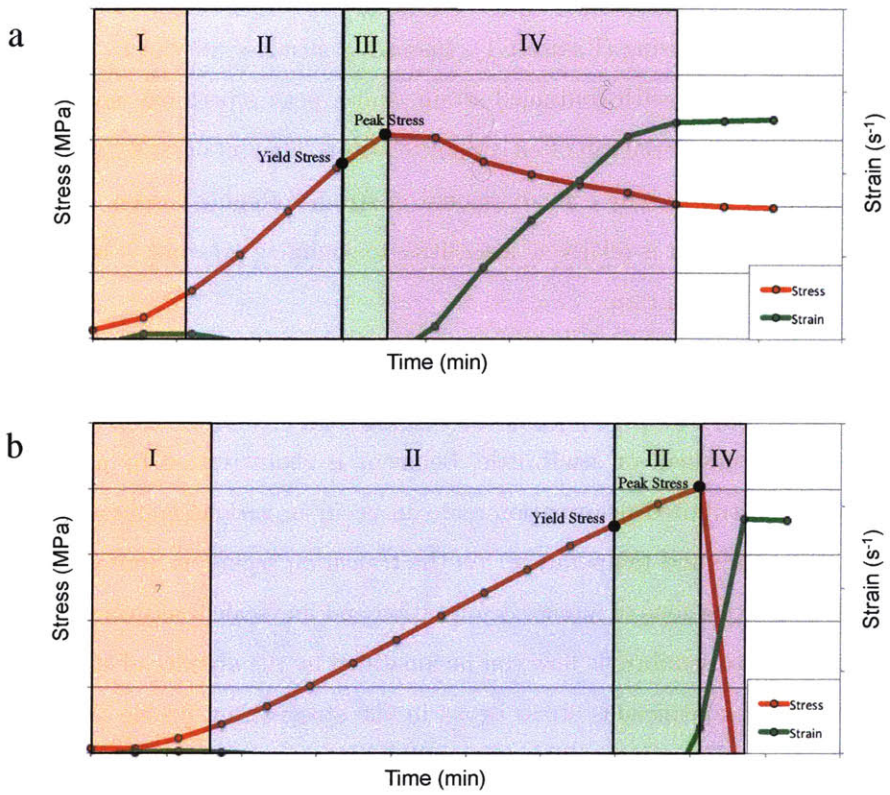

Figure 1-2: The measured stress (red) and calculated strain (green) as a function of experiment time, showing (a) failure with strength retention and (b) catastrophic failure with no strength retention. Since the experiment was conducted under constant displacement rate, the time axis can also be viewed as piston displacement. Stage I: closing of microcracks, Stage 2: linear elastic regime, Stage III: plastic yielding / development of microfractures / strain hardening, Stage IV: slip weakening phase. Both graphs are real data obtained from samples (a) ILS-OD-295 and (b) ILS-WS-150-C.

1.3.2 Ductile Failure

Ductile behavior occurs when a material is able to sustain large strain (high deformation) without macroscopic fracturing. That is, the localization of the microfracturing does not occur as it does in the brittle regime. Typically, ductility may occur in less consolidated materials (granular, poorly lithified), or under high temperature or high confining stress conditions. High temperatures can encourage crystal plasiticity, while high confining stress will serve to suppress brittle behavior.

Ductile deformation involves distributed deformation of the material, where no localized plane can be seen. In addition, the stress-strain profile will not display the sharp stress drop seen in brittle fracturing (Figure 1-1). Instead, a steady-state can be reached wherein continued loading is met with continued strain, and a peak stress may not be reached. If failure is reached, the material can often support the same amount of stress in the post-failure region (Figure 1-1), where only a small amount of strain-softening is seen.

While ductile behavior is relatively insensitive to confining pressure, it is highly sensitive to temperature and strain rate.

1.3.3 Transitional Failure

Brittle-ductile transitional, or semibrittle, behavior is characterized by a combination of localization and distributed deformation and can occur in various materials under certain conditions of pressure and temperature. As the transition regime is approached, the shear failure plane becomes a zone of intense deformation and fine scale fracturing. The transition from brittle failure to semibrittle flow can be identified by the absence of strain localization and the absence of conspicuous stress drops in the stress-strain profile [45]. Like brittle failure, the primary deformation is caused by cataclasis and the behavior is sensitive to pressure.

1.3.4 Strength of Ice

Recent studies on mixtures of ice and rock grains [33] indicate that the compressive strength of the mixture will decrease as the volume fraction of the weak phase (i.e. ice) increases. That is, the more ice that is present, the weaker the aggregate will be, with a minimum strength being the strength of the pure weak phase.

The compressive strength of pure ice is sensitive to both temperature and to confining pressure, but only weakly dependent on strain rate [49]. A study of the inelastic properties of ice Ih [50] indicates a sharp increase in compressive strength with confinement at low confining pressures, followed by a decreased sensitivity at higher confinement. Decreasing temperature also increased the strength, with values of $\sim$70 MPa at 165 K and $\sim$40 MPa at 195 K under 5 MPa of confinement obtained. A more recent study showed similar results [51], with a compressive strength of $\sim$22.5 MPa at 233 K at very low confinement.

While the mechanical strength of ice Ih has been experimentally determined, other phases

with differing crystal structures, grain sizes, and densities will likely have a wide variety of mechanical strengths. In particular, lower density ices like Ih (0.92 to 0.93 g/cm^3) are likely weaker than higher density variants, such as ice VII (1.65 g/cm^3) [31].

Both brittle and ductile behaviors have been observed in the deformation of ice. Lower temperature and higher strain rates promote brittle behavior, while ductile behavior dominates at temperatures greater than 195 K and follows a steady-state flow law [49].

Chapter 2

Methods

2.1 Materials

The two materials chosen for this study were Indiana limestone and Bishop based on their mechanical properties, mineral compositions, and availability.

Though asteroids vary considerably in their composition [52], water-bearing bodies are likely of the carbonaceous chondrite class (CC) [2, 53], comprised mainly of silicates, oxides, sulfates, and the minerals olivine and pyroxene. In order to contain significant amounts of water-ice (not bound in hydrosilicates), porosity is needed (estimates vary from 0% to 30% porosity in CCs [44, 54]). However, as the maximum axial load limit of the experimental apparatus was 200 MPa, it would likely be unable to cause failure in a basaltic rock composed of olivine and pyroxene. Therefore, Indiana limestone was chosen as a suitable sample material due to its availability, porosity ($\sim$15%), low compressive strength at room temperature [55], and its history of use in compressive strength studies [4, 17, 18, 55].

A much softer material, and thus likely deformable by the experimental apparatus, is tuff. Tuff is a light, porous rock made of volcanic ash that forms after deposition of a pyroclastic flow. The Bishop tuff is a middle Pleistocene ash bed that was formed about 0.74 million years ago when a large volume of rhyolite tephra was catastrophically erupted in the Long Valley area of California, over only a few short days [56]. It consisted of two discernible stages; an initial stage in which a large volume of tephra was generated and formed an air-fall pumice unit, and a second ash flow stage that is radially distributed around the source area. During the second stage, enormous volumes of ash were ejected into the atmosphere and formed an ash fall — a blanket-like deposit that covers more than a million square

kilometers of the Western US [56].

The second stage, the sequential, thick ash flows and falls that form the Bishop tuff ash bed, provides a suitable comet/asteroid analog. The tuff primarily consists of quartz, ortho- and clino-pyroxenes, zircon, titanomagnetite, ilmenite, allanite, biotite, oligoclase, apatite, and rhotite [57]. Similarly, carbonaceous chondrites are known from meteorite samples to contain olivine, pyroxenes, and magnetite, while other meteorite types contain examples of most each mineral present in the tuff [58]. Comets, on the other hand, consist mainly of the silicates olivine and pyroxene [59].

Most importantly though, the tuff represents an interesting medium that is neither fully consolidated nor completely granular and unconsolidated. That is, it lies on a spectrum between a very solid rock like the Indiana limestone and an unconsolidated, soil-like regolith. It has a high effective porosity (estimated for the ash flow layer at between 20% and 35%), a total porosity of 35% and 45% [60], and is slightly compacted. A similar material could be found on a planetary body at a depth significant enough to induce slight compaction (the depth at which this could occur would of course be dependent on the size of the body — shallower for a larger body than a smaller one). Our own analysis of the porosity, performed by comparing the calculated bulk density to the density of the constituent grains in the tuff, was in rough agreement with a calculated total porosity from 45% to 55%, indicating a significant amount of intragranular porosity.

2.2 Sample Preparation

Preparation of limestone samples followed typical protocol for tri-axial load experiments [46]. Cylindrical cores obtained from a single large quarried limestone block were machined to the standard core dimensions of 63.5 mm length and 25.4 mm diameter. All samples except for the control were initially heated to 373 K in a vacuum oven for 24 hours to remove as much initial water content as possible. Following the drying process, desiccative storage aided in avoiding reabsorption of atmospheric water. The air-dried (AD) control sample, which remained at laboratory conditions, consequently retained its original water content.

Large pieces of the Bishop tuff were obtained from the Chalfant Quarry near Bishop, California. Figure 2-1 shows the location of the samples. The pieces were then cut into bricks and, due to the extremely soft nature of the rock, hand sanded into rough cylinders. These

cylinders were then carefully ground to a constant 25.4 mm diameter and subsequently cut to 63.5 mm length, with the ends made as parallel as possible.

To minimize thermal shock, samples of both limestone and tuff to be tested at low temperatures (240 K, 150 K, or 77 K) underwent a two-step freezing process. First, samples were placed in a freezer and allowed to adjust to the ambient 238 K temperature for at least two hours. Meanwhile, the cryogenic rig was cooled to the desired testing temperature. Subsequent transfer of the test sample into the cooled rig allowed for a minimum of 1.5 hours equilibration to the testing environment.

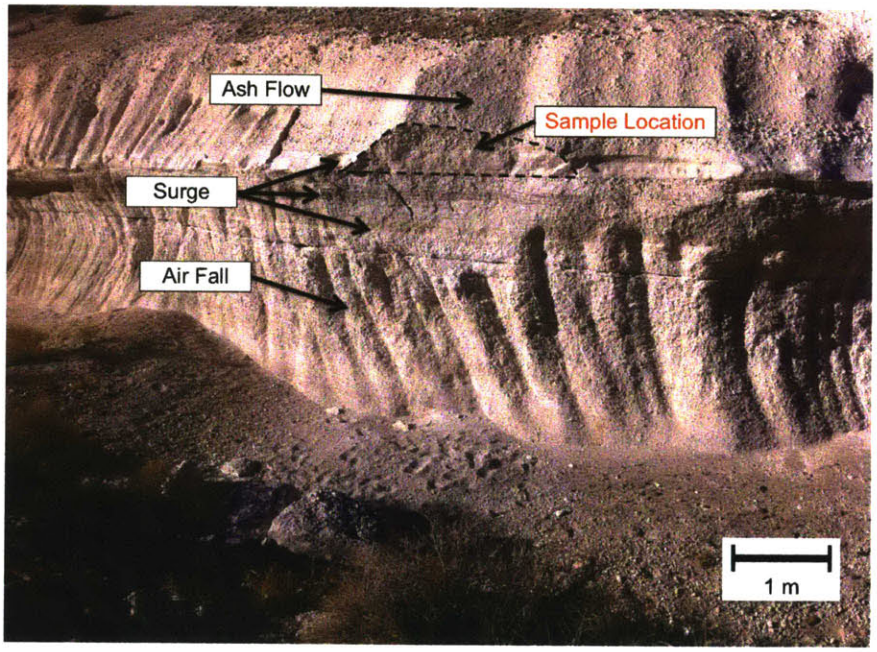

Figure 2-1: Location where Bishop tuff samples were acquired at Chalfant Quarry in Bishop, California. Large blocks were taken from the region encompassing the ash and surge flows.

Saturation

While all limestone samples underwent initial oven drying (designated OD), only three of the samples were to be tested as such. These samples were left in a dessicator at room temperature while awaiting testing.

Saturation of limestone samples destined to be water-saturated (WS) occurred by vacuum imbibition. The limestone cylinders were placed inside vacuum tubes and connected to a vacuum pump. After initial evacuation, the tubes were backfilled with deionized and

degassed water, ensuring as much of the pore space was saturated as possible.

Two saturation states were intended for the tuff samples: air-dried and water-saturated. Little additional preparation was done on the air-dried samples aside from ensuring the ends were completely parallel. This was performed using a special cylindrical jig initially developed at MIT. The jig allows a cylindrical sample to be held in place while a razor is used to scrape away small amounts of material at the sample ends. As the ends of the jig are completely parallel, so too are the resulting ends of the sample.

Saturation of the tuff was a difficult process that required multiple attempts in order to avoid complete sample destruction.

Similar to the limestone, the tuff samples (left slightly longer than 63.5 mm) were placed in vacuum tubes and connected to a vacuum pump. Once under vacuum, deionized and degassed water was passed through the samples, with the intent of occupying all of the pore space. Difficulty occurred when the granular edges of the tuff samples stuck against the cylinder walls, causing the upper portions of the samples to fail in tension. This resulted in samples that had considerable horizontal, ice-filled fractures.

Suitable samples were created by sanding down the sample edges to slightly below 25.4 mm, preventing the granular edges from catching on the tube walls and ensuring no failure in tension.

Once saturated, all samples (limestone and tuff) were left within the vacuum tubes and placed in a freezer to be kept at 243 K overnight. As the tubes were on a copper plate, freezing occurred from the bottom up and any trapped gases were forced to the top of the sample. This reduces the potential for air bubbles to form in the pore spaces of the sample, likely reducing the overall compressive strength by serving as points of weakness (or weakening by having some pore spaces filled with air rather than ice).

Using the same jig as described for the air-dried samples, the resulting frozen cylinders of tuff and ice were shaved down to 63.5 mm with parallel ends.

2.3 Experimental Procedure

Following equilibration to the testing environment, sample loading began. The compressive strength of the samples was determined using the apparatus and techniques developed by Durham, Heard, and Kirby [49]. The experiment ran at a constant displacement rate of

0.004 mm/s, which for a 63.5 mm diameter sample results in a strain rate of $\sim$6.3 x 10^{-5} s^{-1}.

While the unconfined compressive strength (UCS) is a desirable property to be measured, there is often uncertainty in obtaining UCS measurements. This uncertainty is often due to pre-existing microcracks in the sample, which can be closed upon application of a small amount of confining pressure and the scatter in the data reduced [46]. For all temperatures, nitrogen gas provided confining pressure (5 MPa for most experiments, except for two which will be discussed in Chapter 3), and thin indium sleeves jacketed the samples.

Due to timing and availability of material, no effort was made to determine error associated with the limestone samples, as only one experiment was run at each testing point. However, results from previous studies [17] indicate an error of +/− 12 MPa, based on five repetitions, is reasonable (see Figures 3-1 and 3-2). For the Bishop tuff, three samples tested at 150 K provide an error estimate of +/− $\sim$20 MPa, and will be discussed in more detail in Section 3.2. More accurate error estimates can be made with additional repetition, ideally ten or more, though it is often practically infeasible due to limited sample availability and time.

Determining Ultimate Strength

A force gauge connected to the sample assembly records in millivolts the differential load (axial load provided by the piston minus confining pressure provided by the nitrogen gas) on the sample while the piston is displaced upward at a constant rate. Displacement continues until a spike in the recorded load is seen, which indicates that the piston has contacted the sample.

Once initial contact occurs, the piston is again displaced upward, and the measured load is observed. The sample is stressed until failure occurs, wherein a drop in the load is seen, or until the load capacity of the apparatus is reached. If the sample fails completely, no load is supported and the experiment is completed. However, if the sample is still able to support a load, additional displacement can help to determine the strain-weakening portion of the stress curve (see Figure 1-2).

Data correction is necessary in order to convert the recorded data (load and displacement) into stress and strain measurements. Detailed information on these corrections can be found in Appendix A.

Chapter 3

Compressive Strength Experiments

In this chapter, we determine the compressive strength of both Indiana limestone and Bishop tuff under dry and saturated conditions, and at cryogenic temperatures. From this, we obtain the temperature dependence of compressive strength for the comet and asteroid analogs .

Additional experiments provide insight on the effects of thermal cycling, reloading, and increased confining pressure on the compressive strength.

3.1 Indiana Limestone

3.1.1 Results

Samples, saturations, testing temperatures, and ultimate strengths are provided as Table 3.1, and the results can be seen graphically in Figure 3-1. What is immediately noticeable is that a decrease in temperature caused a significant increase in compressive strength of the water-saturated samples (WS), while no significant increase in strength was observed in the oven-dried (OD) samples.

At 240 K, the water-saturated (ILS-WS-240) ultimate strength was 94 MPa, an increase in strength of 62 MPa compared to the air-dried control sample (ILS-AD-295). At 150 K and 77 K, the saturated samples (ILS-WS-150 and ILS-WS-77, respectively) were so strong that the apparatus was unable to provide sufficient load to cause them to fail. Therefore, though their peak stress is in excess of 200 MPa under 5 MPa of confining stress, the exact strength of both samples cannot be determined.

The limestone samples showed evidence mainly of brittle deformation, with an initial

linear elastic response followed by a non-elastic phase, final yielding, and slip-weakening in the post-failure regime (Figure 1-2), as described in Section 1.3. However, sample ILS-WS-240 has a stress profile that may indicate brittle-ductile transitional behavior (see Figure B-2).

Sample	Confining Pressure (MPa)	Temperature (K)	Saturation State	Thermally Cycled?	Ultimate Strength (MPa)
ILS-AD-295	1	295	AD	N	32
ILS-WS-240	5	240	WS	N	94
ILS-WS-150	5	150	WS	N	200+
ILS-WS-77	5	77	WS	N	200+
ILS-OD-295	5	295	OD	N	59
ILS-OD-150	5	150	OD	N	79

Table 3.1: Experimental results from compressive strength tests on Indiana limestone under air-dried (AD), oven-dried (OD), and water-saturated (WS) conditions. ILS-AD-295 is considered the control sample. An increase in strength with decreased temperature is apparent for fully saturated samples.

3.1.2 Interpretation

The compressive strength experiments on Indiana limestone provide insight into the behavior of water-saturated, consolidated rock at low temperatures. Three important conclusions can be drawn from the results:

1. *The presence of ice in pores can significantly increase the strength of the saturated material at low (cryogenic) temperatures.*

   Comparison of the control sample to ILS-WS-240, ILS-WS-150, and ILS-WS-77 indicates that the presence of ice in the pore space of the limestone samples serves to increase the strength significantly. An overall strength increase of greater than 100 MPa was observed between ILS-WS-240 and ILS-WS-150, which is a strengthening of slightly more than a factor of two. However, since it is known that water in the pores of a limestone will weaken it at room temperature (due either to the reduction of surface energy at the crack tip [61] or stress corrosion effects [62]), we would expect the water-saturated strength at 295 K to be less than that of the control. An overall strengthening of more than 170 MPa (<35 MPa to >200 MPa) is observed, which is at least a four-fold increase in strength from room temperature to 150 K or 77 K.

   The slight increase in oven-dried strength between ILS-OD-150 and ILS-OD-295 may be well within experimental error (see Figure 3-1). There does not seem to be a viable

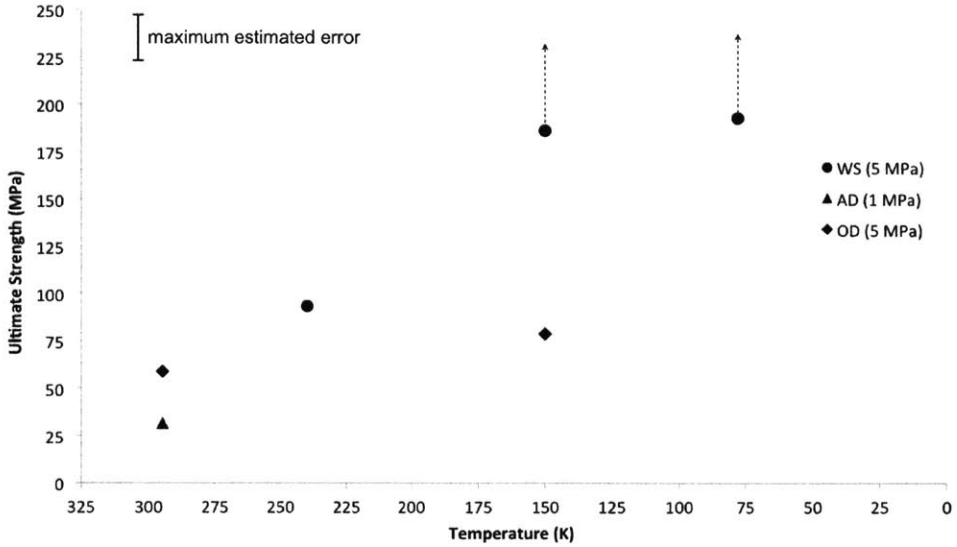

Figure 3-1: Graphical representation of the experimental results of compressive strength tests on Indiana limestone. Air-dried (AD), oven-dried (OD) and water-saturated (WS) samples were subjected to compression at various temperatures. A decrease in temperature results in a large strength increase for the saturated samples, and relatively little increase for the air-dried samples. Note that water-saturated samples at 150 K and 77 K did not fail, therefore the maximum load achieved is represented by the dot and the dashed arrow indicates that the ultimate strength resides at a larger value. The maximum estimated error is based on the work of Mellor in 1971 [17] (see also Figure 3-2).

explanation for the increase in strength of a dry rock, aside from arguments considering the thermal expansion of various grain types. The samples in this study, being relatively homogeneous Indiana limestone, should have minimal variation in grain type. However, no previous study has been done on the low-temperature dependence of oven-dry rock.

2. *A small amount of confining pressure can significantly increase the strength of a saturated material.*

   Comparison of the results of this study to that of previous studies on the unconfined compressive strength [17] (Figure 3-2) demonstrates that a small amount of confining pressure can significantly increase the strength of the saturated rock. The maximum unconfined compressive strength achieved in the previous study was ~175 MPa and occurred at 150 K, while samples ILS-WS-150 and ILS-WS-77 in this study exceeded

200 MPa at both 150 K and 77 K (at 5 MPa confining pressure). The increase seen in this study is likely the result of the higher confining pressure.

Potential transitional behavior observed at 240 K will be further discussed in Section 3.4.

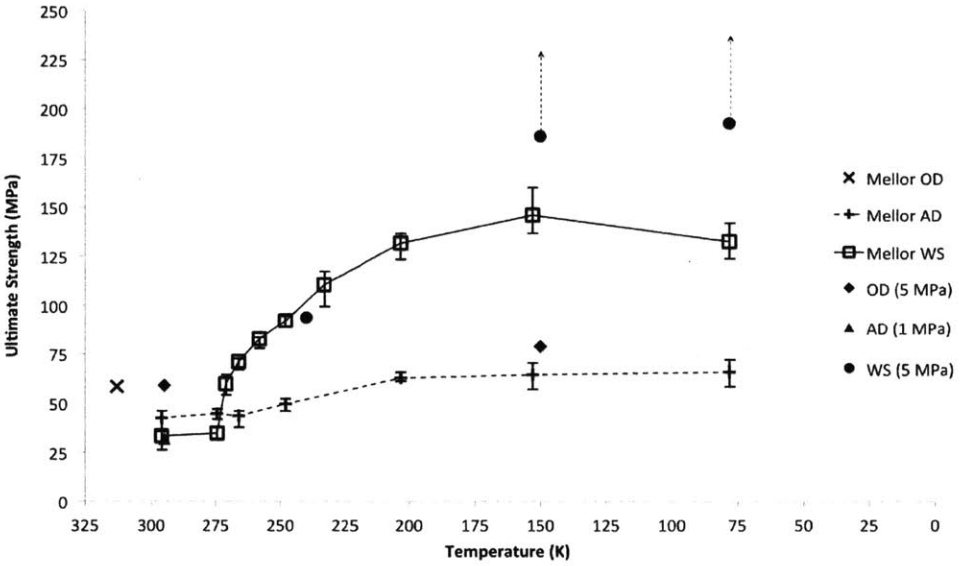

Figure 3-2: Comparison of the results of this study on Indiana limestone with those of Mellor (1971) [17], who determined the unconfined compressive strength of the limestone (saturated, oven-dried, and air-dried) at cryogenic temperatures. An increase in strength is seen for samples under higher confining pressure, except for a notable saturated sample at 240 K. Note that the error estimates of Mellor's measurements are based on five replications.

3.2 Bishop Tuff

3.2.1 Results

Samples, saturations, testing temperatures, and resulting ultimate strengths can be seen in Table 3.2 and Figure 3-3. What can immediately be seen is that a decrease in temperature causes a significant increase in the compressive strength of the saturated tuff, while no change is seen in the air-dried samples.

To start, an initial room temperature, air-dried strength measurement (control sample) was required. This serves as a base point or control sample for comparison of the later

Sample	Confining Pressure (MPa)	Temperature (K)	Saturation State	Ultimate Strength (MPa)
BT-AD-295(1)	5	295	AD	13
BT-AD-295(2)	5	295	AD	14
BT-WS-240	5	240	WS	26
BT-WS-200	5	200	WS	62
BT-WS-150(1)	5	150	WS	179
BT-WS-150(2)	5	150	WS	164
BT-WS-150(3)	5	150	WS	138
BT-SI-150	5	150	SI	65
BT-AD-150	5	150	AD	15

Table 3.2: Experimental results from compressive strength tests on Bishop tuff under air-dried (AD) and water-saturated (WS) conditions, as well as one standard ice (SI) sample. Note that samples BT-WS-150(1-3) were used to determine the error associated with the experiment (see Figure 3-3).

results at lower temperatures. As before, 5 MPa of confining pressure was used to reduce noise in the data.

The control samples (BT-AD-295(1) and (2)) had ultimate strengths of 13 MPa and 14 MPa under 5 MPa of confining stress. This indicates that the tuff is quite soft, which became obvious during the sample collection and preparation. As Figure 3-4 shows, the linear strain profile and the shape of the stress curve (along with the deformation characteristics) indicate ductile failure, and that cataclasis is the dominant failure mechanism.

If 200 K is a transitional temperature between the ductile and brittle fields, we should expect lower temperatures to exhibit more brittle behavior. That is indeed the case, as the experiments at 150 K show (Figure 3-4, sample BT-WS-150(2)). The water saturated samples (three samples were run at 150 K to produce an estimate of error) all show brittle failure, with the classic stress profile and axial fractures described in Section 1.3. High strengths were recorded for these samples (BT-WS-150(1-3)): 179 MPa, 164 MPa, and 138 MPa respectively. The resulting average value and associated error at this temperature is therefore 160 +/− 20 MPa. The calculated error bar is indicated in Figure 3-3.

Additionally, both a sample of standard ice [49] (BT-SI-150) and an air-dried tuff sample (BT-AD-150) were prepared and tested at 150 K and under 5 MPa of confining pressure to provide the compressive strengths of the individual components of the saturated tuff. Neither the standard ice (ultimate strength of 65 MPa) nor the air-dry (15 MPa) come close to the strength of the ice-tuff mixture.

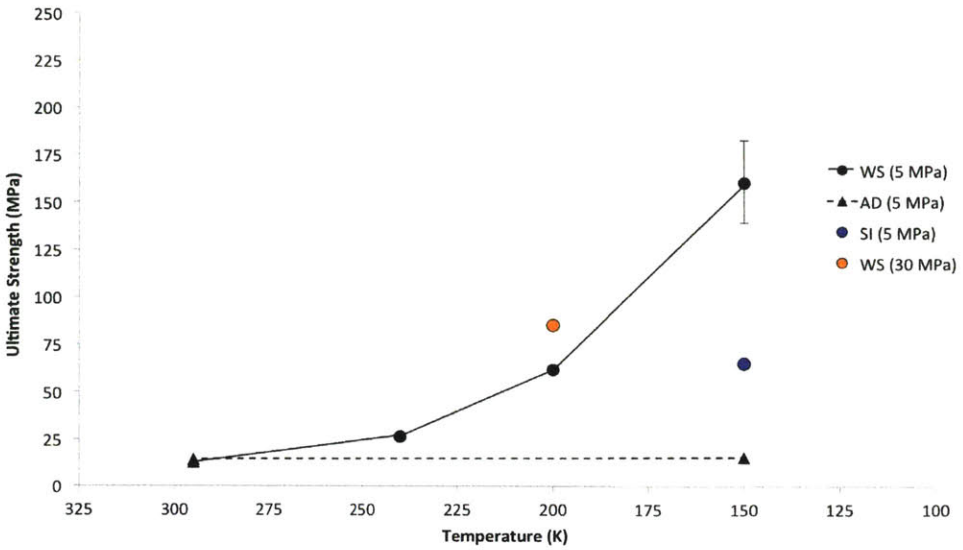

Figure 3-3: Graphical representation of the experimental results of compressive strength tests on Bishop tuff. Air-dried (AD) and water-saturated (WS) samples were subjected to compression at various temperatures. A decrease in temperature results in a large strength increase for the saturated samples, and no increase for the air-dried samples. A sample of standard ice (SI) was tested at 150 K (blue circle), as well as a single sample at elevated confining pressure (30 MPa, orange circle) which will be discussed in more detail in Section 3.4. Note that the error bar is based on three samples all run under the same conditions at 150 K.

3.2.2 Interpretation

The experiments provide insight in to the behavior of a water-saturated, semi-consolidated granular material at cryogenic temperatures. Three important conclusions can be drawn from the results:

1. *The presence of ice in pores can significantly increase the strength of the saturated material at low (cryogenic) temperatures.*

   Comparison of the air-dried tuff at room temperature to the water-saturated samples at 240 K, 200 K, and 150 K show a clear trend of non-linearly increasing strength. The air-dried samples do not show a significant increase in strength between 295 K and 150 K, which is to be expected, as no ice exists in the pore space to provide the additional support.

2. *The presence of ice within the pore space of a porous material will result in a composite*

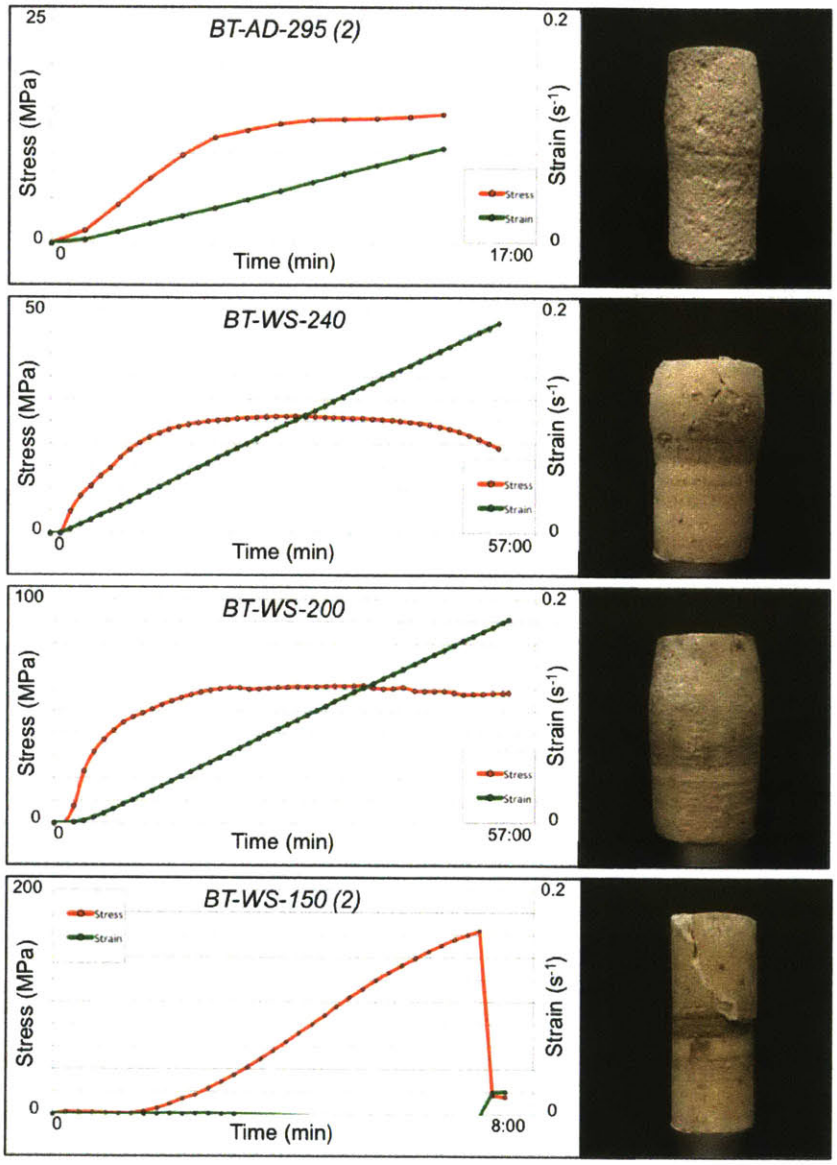

Figure 3-4: A comparison of the stress (red) and strain (green) profiles and deformation characteristics of four Bishop tuff samples at various temperatures. The stress curves and deformation characteristics indicate a transition from ductile (BT-AD-295 (2)) through transitional (BT-WS-200) to fully brittle (BT-WS-150 (2) behavior.

material that is stronger than either of its individual constituents.

As is seen in Figure 3-3, the strength of the tuff itself at 150 K and under 5 MPa of confining pressure is 15 MPa and the strength of ice itself is 65 MPa. However, the combination of the two (a saturated tuff sample) at the same temperature has a

strength of 160 MPa. This means that the composite material — tuff and ice — is almost 100 MPa (~146%) stronger than the strongest constituent material.

Considering the fact that the dry tuff can be seen as a composite material composed of tuff and air in the pore spaces, the result is consistent with expectations. Replacement of the air with a much stronger material (ice) results in a much stronger composite.

3. *Brittle-ductile transitional behavior occurs between 240 K and 150 K for a saturated granular material.*

   The stress and strain characteristics of the air-dried sample at 295 K and the water-saturated sample at 240 K show distinctly ductile failure, with a very short initial elastic phase proceeded by a long yielding phase (accompanied by almost constant straining, Figure 3-4). At 200 K, however, the water-saturated sample begins to have a much more pronounced elastic region at the onset of loading, with strain being delayed until the yielding portion begins. This indicates a transition into the brittle field, which is exemplified by the stress and strain profile of the water-saturated sample at 150 K.

   Furthermore, the deformation characteristics of the samples support the hypothesis that a transition is seen from the ductile to brittle fields. The air-dried sample at 295 K shows evidence of cataclasis, as does the water-saturated sample at 240 K, though some axial fractures are evident. At 200 K, the sample still appears to have distributed deformation without any visible localized fractures, but by the time 150 K is reached the failure is almost entirely brittle within a highly localized plane (Figure 3-4).

Finally, a comparison of the tuff behavior to previous studies on ice under high confining pressure and low temperature [50] (Figure 3-5) shows a strong similarity in the overall trend. This may indicate that the behavior of ice plays a dominant role in the combined material of ice and tuff, with the tuff providing the general increase in strength.

3.3 Summary of Main Experiments

The experiments discussed here provide fundamental information for future space programs and planetary surface analysis.

Material such as tuff is likely present on many bodies in the solar system, specifically

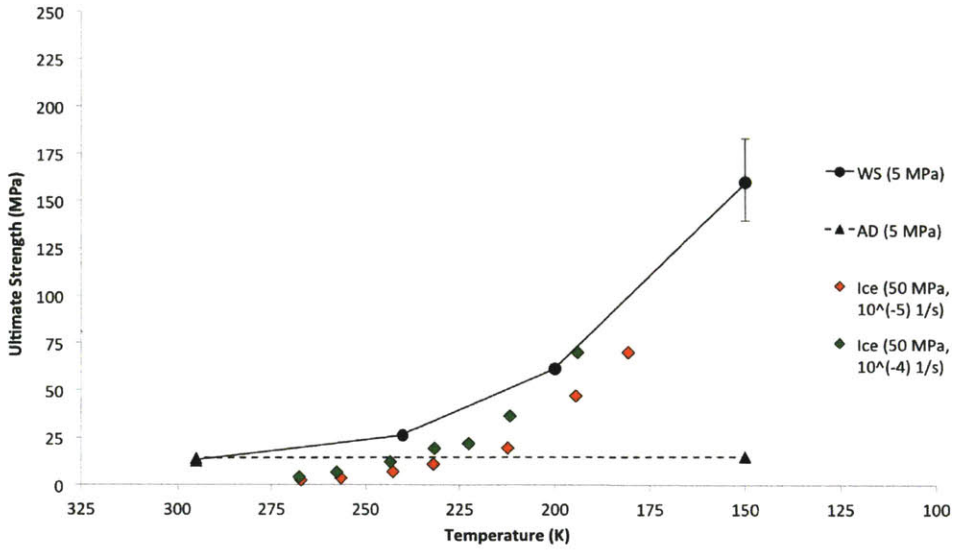

Figure 3-5: Comparison of the compressive strength of saturated Bishop tuff samples to standard ice under high confining pressures (50 MPa) and similar strain rates (the strain rate of this study is 6.3 x 10^{-5} s^{-1}). Similarity in the trends indicates that the behavior of ice dominates the composite material.

those that are tectonically and geologically active. As relatively unconsolidated as the Bishop tuff is, we speculate that similar material could be found near the surface of planets or asteroids. Carbonates, while not present on other bodies as they are on Earth (sedimentary rocks formed from the carbonaceous shells of aquatic animals), do exist on asteroids [58] and calcite is a very common mineral in our solar system. Other materials of a similar density and porosity likely exist as well, allowing limestone to serve as a suitable analog for behavioral studies.

The significant increase in compressive strength seen in both the saturated limestone and saturated tuff due to a decrease in temperature is of utmost importance to future sampling missions. Energy considerations for drills are highly dependent on the compressive strength of the material to be penetrated [63], as described by the specific energy (SE) [4]:

$$SE = \frac{W_{drilling}}{ROP \cdot A} \tag{3.1}$$

where $W_{drilling}$ is the power consumed during drilling (in J/s) — a function of weight on bit, rotational speed, and torque), ROP is the rate of penetration of the drill bit into

the substrate (in m/s), and A is the cross-sectional area of the resultant borehole (in m^2). Specific energy is a complicated function that involves many variables related to both the physical properties of the medium being drilled and to the drilling method itself [4, 63], and is measured in units of energy per unit volume (J/m^3) or stress (Pa). It has been observed that the minimum specific energy of a material is often quite similar to the unconfined compressive strength (UCS) of that material [63], which indicates that UCS may be directly related to the maximum efficiency of drilling a substrate. However, the relationship between specific energy and UCS is not currently known. One can observe a correlation between the two (Figure 3-6) if all the drilling variables are held constant and only UCS is altered. Note that in the case of confined compressive experiments, the UCS can be estimated from the confined compressive strength using Mohr analysis [64] (UCS is equivalent to the cohesion parameter).

Knowledge of the strength of the material is therefore critical in predicting the energy required to penetrate it with a drill bit. In Chapter 4, specific energies for materials such as the Indiana limestone and Bishop tuff will be calculated and compared to current mission equipment. Lander harpoons will also need an estimate of the substrate strength to optimize the velocity at which they are ejected.

The ductility of a substrate is also of paramount importance, and the transitional behavior observed at 200 K is critical to the prediction of substrate behavior for landers, drilling, and geomorphology. The strengthening effect of confining pressure also gives insight into the material properties at depth in planetary bodies, beneath the penetration depth of our remote sensing tools.

3.4 Additional Experiments

In addition to the main set of experiments previously described, which aimed at characterizing the effect of temperature on the compressive strength of two porous planetary analogs, three more experiments were performed to address the effects of thermal cycling, sample reloading, and significantly increased confining pressure.

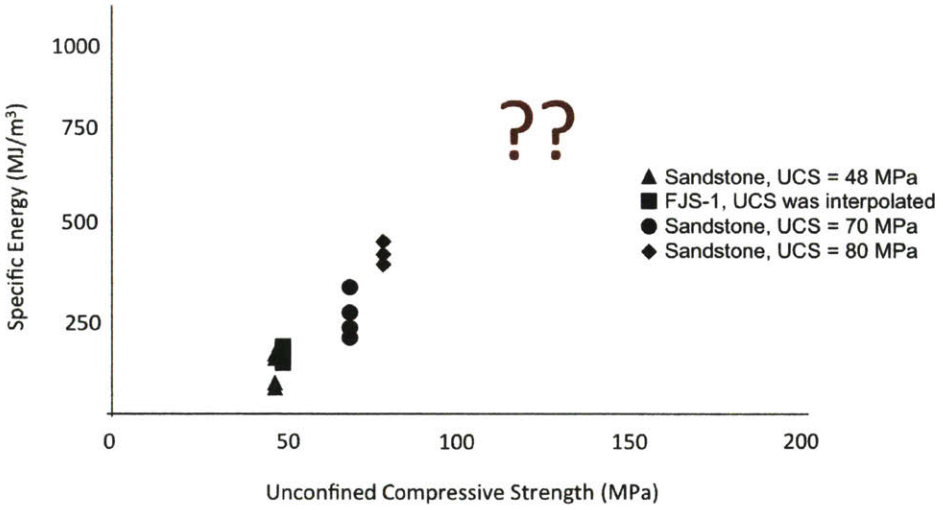

Figure 3-6: Specific energy of various sandstones and a lunar simulant as a function of UCS (from [4]), and the unknown extension to higher strength materials.

3.4.1 Amended Experimental Procedures

Thermal Cycling

Thermal cycling tests were run on the Indiana limestone and involved subjecting both a saturated and oven-dried sample to one freeze-thaw cycle (ILS-WS-150-C and ILS-OD-150-C, respectively), and then compressing until failure at 150 K.

After the initial saturation and cooling of two limestone samples as described in Chapter 2, the samples were both allowed to thaw out over a period of 24 hours. Once equilibrium with room temperature was reached, both samples were placed in a vacuum oven for another 24 hours to remove as much water as possible from the pore space.

One sample was then re-saturated and re-cooled using the aforementioned technique. The second sample, to be tested dry, was placed into a sealed bag after drying. Both samples were left to cool for 24 hours in the freezer, as before.

Both the saturated and the oven-dried cycled samples were tested under the same conditions of temperature, confining pressure, and displacement rate as their non-cycled counterparts (150 K, 5 MPa, and 0.004 mm/s respectively). This allows for an easy comparison between the resulting compressive strengths.

Reloading

The reloading (loading until failure, unloading, and then reloading under the same conditions) of a single water-saturated limestone sample was investigated at 240 K (sample ILS-WS-240*).

In this experiment, the intent was to observe the effect of reloading of a sample that had previously failed (ILS-WS-240). The initial sample, water-saturated at 240 K, displayed potential transitional behavior in both its stress-strain profile and its deformation (Figure B-2). By reloading the sample, the transitional nature can be observed and confirmed, as brittle failure would result in a lack of load support while ductile failure would allow for continued support of loads near the peak stress.

After the initial failure of the water-saturated limestone sample at 240 K, it was placed once more into the apparatus and tested again (ILS-WS-240*) at the same experimental conditions as the initial run.

Elevated Confining Pressure

In this experiment, the effect of increased confining pressure on a sample of the saturated tuff at 200 K was investigated. Transitional behavior was observed at this temperature (see Section 1.3), and an increase in confining pressure will help to determine the extent of brittle failure. Recall from Section 1.3 that the brittle regime is sensitive to confining pressure while the ductile regime is not, and that an increase in confining pressure serves to inhibit brittle failure.

A water-saturated sample of tuff, prepared as described in Chapter 2, was tested under similar conditions of temperature (200 K) and displacement rate (0.004 mm/s). The confining pressure, however, was increased to 30 MPa using nitrogen gas.

3.4.2 Results

Thermal Cycling

The experimental results can be seen in Table 3.3 and Figure 3-7, along with the non-cycled counterparts described in Section 3.1.

As expected, the cycled samples were weaker than the non-cycled samples at the same testing conditions. The oven-dried sample (ILS-OD-150-C) was weaker by 6 MPa than its

Sample	Confining Pressure (MPa)	Temperature (K)	Saturation State	Thermally Cycled?	Ultimate Strength (MPa)
ILS-AD-295	1	295	AD	N	32
ILS-WS-240	5	240	WS	N	94
ILS-WS-240*	**5**	**240**	**WS**	**N**	**60**
ILS-WS-150	5	150	WS	N	200+
ILS-WS-77	5	77	WS	N	200+
ILS-WS-150-C	**5**	**150**	**WS**	**Y**	**198**
ILS-OD-295	5	295	OD	N	59
ILS-OD-150	**5**	**150**	**OD**	**N**	**79**
ILS-OD-150-C	**5**	**150**	**OD**	**Y**	**71**

Table 3.3: Additional compressive strength experiments (highlighted in black) performed on Indiana limestone in this study. The previously discussed experiments are indicated in gray. Samples with a "-C" indicate one thermal cycle, while the sample with a "*" indicates reloading.

non-cycled counterpart (ILS-OD-150), and the water-saturated sample (ILS-WS-150-C) was compressed to failure, with an ultimate strength of 198 MPa.

The stress-strain profiles of both samples, along with their deformation characteristics, can be seen in Figure 3-7. In comparison with the non-cycled counterparts (Figure 3-8), it is obvious that the strain profiles are little changed. The only difference is the reduced strength and, in the case of the oven-dried cycled sample, a slight increase in the strain-softening phase post-failure.

Reloading

Upon reloading of the sample, it showed immediate evidence of strain while the stress profile built to a peak stress of 60 MPa (see Table 3.3). Failure then occurred and the sample began to strain-soften until displacement was stopped (Figure B-7). Once removed, localized failure was apparent in the upper portion of the sample, indicating brittle failure. However, comparison of the initial stress-strain profile (Figure 3-9) with the reloaded profile shows that the peak stress reached was the steady-state post-failure stress of the initial sample, indicating ductile behavior.

Elevated Confining Pressure

The sample (BT-WS-200-30), under the additional confining pressure, achieved a higher ultimate strength than sample BT-WS-200 at 5 MPa (Table 3.4 and Figure 3-10): 85 MPa and 62 MPa respectively. While the increase in strength was expected, the stress-strain

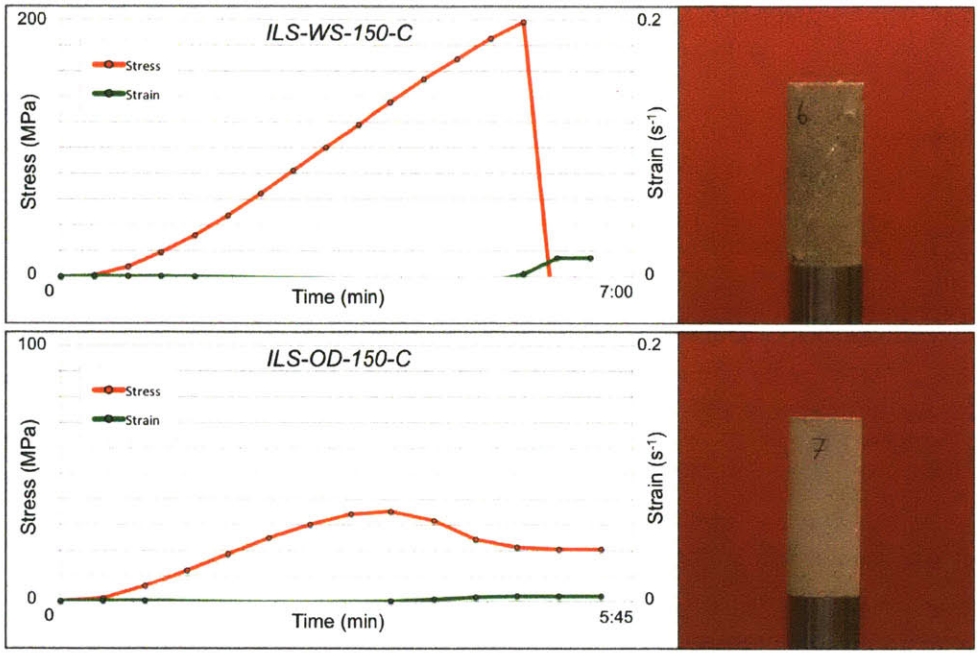

Figure 3-7: Comparison of the stress-strain profiles and deformation characteristics of thermally-cycled Indiana limestone samples at 150 K. Both samples were weaker than their non-cycled counterparts.

profile of the two samples is strikingly similar, showing an initial elastic response followed by a near steady-state stress response to almost linear strain.

The deformation of the two, however, is quite different (as seen in Figures C-3 and C-9). The 5 MPa sample shows a more barrel-shaped deformation, while the 30 MPa sample displays the narrow waste typical of 100% ice ductility and a more rumpled jacket, all indicating ductile behavior.

3.4.3 Interpretation

Thermal Cycling

The decrease in strength seen in the thermally cycled samples is expected, and the results of the experiment confirm that, even at low temperatures, freeze-thaw cycles can weaken both saturated and dry consolidated rock.

Thermal cycles weaken the material by progressive microfracturing due to the crystallization pressure of ice growth during freezing [65] and the subsequent removal of the

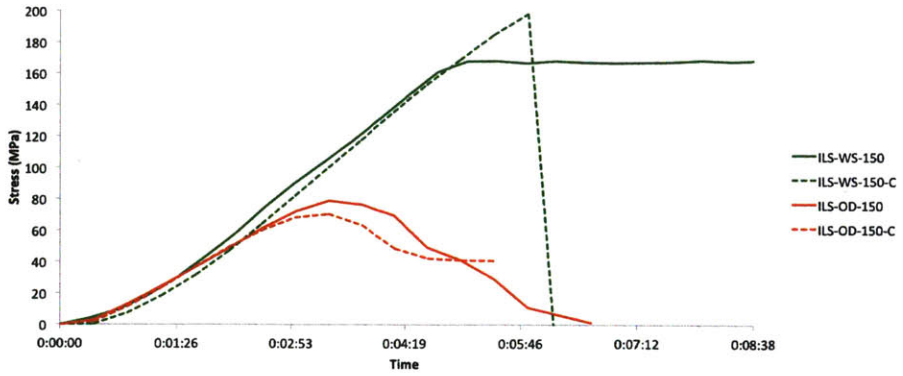

Figure 3-8: Comparison of the stress-strain profiles of the cycled (-C, dashed lines) and non-cycled (solid lines) oven-dried (OD, red) and water-saturated (WS, green) limestone samples. Both cycled samples were weaker than their non-cycled counterparts.

Sample	Confining Pressure (MPa)	Temperature (K)	Saturation State	Ultimate Strength (MPa)
BT-AD-295(1)	5	295	AD	13
BT-AD-295(2)	5	295	AD	14
BT-WS-240	5	240	WS	26
BT-WS-200	5	200	WS	62
BT-WS-200-30	**30**	**200**	**WS**	**85**
BT-WS-150(1)	5	150	WS	179
BT-WS-150(2)	5	150	WS	164
BT-WS-150(3)	5	150	WS	138
BT-SI-150	5	150	SI	65
BT-AD-150	5	150	AD	15

Table 3.4: Additional compressive strength experiment (highlighted in black) performed on Bishop tuff in this study. The previously discussed experiments are indicated in gray.

load-bearing ice via oven-drying eliminates the strengthening effect of the ice. Thus the decrease in strength of the oven-dried sample is explained, as the cycled sample now contains more microcracks due to the initial freezing.

Upon re-saturation, however, one could expect that entry and subsequent freezing of ice into the initial microfractures would negate the weakening effect. In this experiment a weakening effect is still seen, though it is impossible to tell how significant the effect is due to the inability to cause failure of the non-cycled sample.

Reloading

The contradictory nature of the results indicates that the sample has experienced transitional behavior. While the final deformation shows localization of failure along a clearly-defined

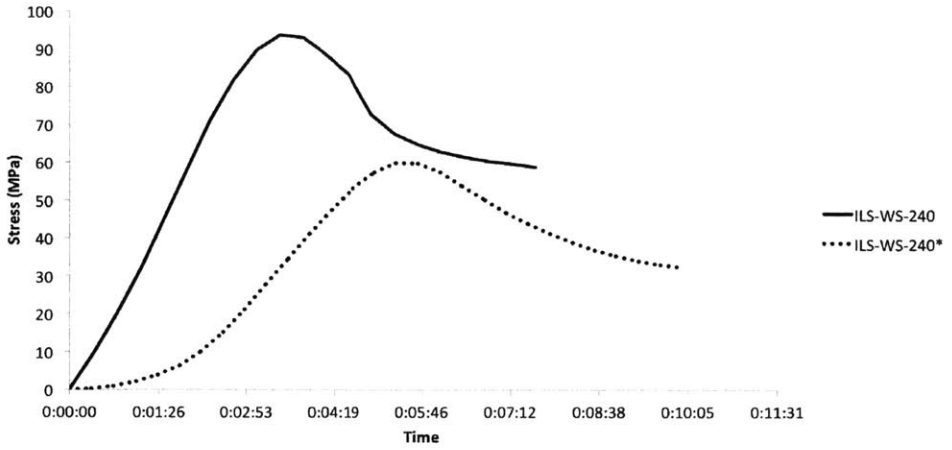

Figure 3-9: Comparison of the stress profiles of two limestone samples at 240 K. The dotted line represents the reloaded sample, while the solid line represents the original sample. Note that the maximum strength of the reloaded sample(ILS-WS-240*) is approximately equal to the final post-failure strength of the original (ILS-WS-240).

plane, the stress-strain profile indicates ductile behavior with immediate strain and a peak stress equivalent to the steady-state stress of the original sample.

These contradictions can be explained by the fact that reloading of the sample caused ~3% total strain, which is the defined amount that a semibrittle material can sustain before failure [45]. Therefore, the sample was strained enough that localized failure occurred even though the behavior was in the semibrittle regime.

Elevated Confining Pressure

The increase in confining pressure, from 5 MPa to 30 MPa, increased the strength of the material while also inhibiting brittle failure, resulting in more ductile behavior. The result supports the concept that the saturated tuff is experiencing transitional behavior between the brittle and ductile regimes at this temperature. The results of the saturated tuff at 150 K indicate that the material is firmly in the brittle regime, while at 240 K and warmer ductile behavior dominates.

Considering the fact that ice is known to have almost entirely ductile behavior at temperatures warmer than 195 K [49] (the only brittle behavior occurring at low confining pressure), and transitional behavior at 195 K, the results of this experiment indicate that the ductility of ice may be the dominant constituent in the overall behavior of the saturated

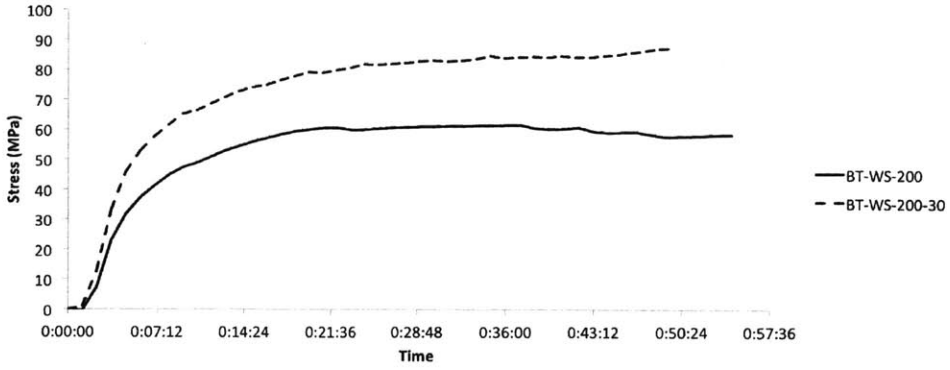

Figure 3-10: Comparison of the stress profiles of two saturated Bishop tuff samples, one under 5 MPa of confining pressure (BT-WS-200, solid line) and one under 30 MPa (BT-WS-200-30, dotted line). The additional confining pressure caused a significant increase in compressive strength.

tuff.

The increase in strength due to increased confining pressure, on the other hand, is likely due more to the behavior of the tuff than the ice, as ice is known to be weak under even greater confining pressure (~7 MPa strength at 50 MPa confining pressure) [66].

3.4.4 Summary of Additional Experiments

The experiments described in this section serve to further our understanding of how these two planetary analogs — a consolidated limestone and a less consolidated tuff — could behave under various planetary conditions.

Thermal cycling is a process well known to alter planetary surfaces, including asteroids, Mars, and of course the Earth [67, 65, 68]. Through progressive fracturing of surface material, it could even be a dominant method of "rubblizing" regolith. It is shown here that, even when saturated with water, thermal cycling still has the effect of reducing the compressive strength of a consolidated limestone.

Ductility and brittleness have extremely important roles to play in how material behaves under certain conditions of pressure and temperature. By reloading a failed saturated limestone sample, it is shown that, at 240 K, the material can still support a significant load before failing again. However, significant strain (3%+) could cause localization of the failure plane, and fracturing will begin.

Elevated confining pressure — more suitable to the study of the interior of larger planetary bodies where overburden or tectonic pressures may dominate — will increase the compressive strength of water-saturated material. Ductility, however, will be encouraged at temperatures near 200 K and warmer.

From spacecraft landers using harpoons to penetrate the near-surface, subsurface drills attempting to access pristine planetary material, to the geomorphology of planetary surfaces, the strengthening and weakening effects described here are important considerations.

Chapter 4

Discussion

The work performed in this study on the compressive strength of asteroid and comet analogs and others involving ice/rock aggregates [33] support the assertion that the increase in ice strength is the dominant factor in the overall strengthening of the studied materials, and that the presence of ice on planetary, cometary, or asteroidal bodies is an important factor to consider when planning extraction or landing maneuvers [69].

Our findings begin to probe the fundamental questions that current and future space explorers will face. How do we extract material from extraterrestrial bodies? How hard or soft will the substrate be? What technologies will we need, and how much energy will be required to extract the resource? How do we land on and anchor to the body? The questions are legion, and many new missions being prepared have sample acquisition as the primary goal [1] (eg. the Comet Surface Sample Return and the South Pole-Aitken Basin Sample Return missions).

The increase in strength observed in saturated porous materials — both consolidated and semi-consolidated — at low temperatures demonstrates the need for a detailed understanding of the mechanical properties of the saturated substrate of a potential extraterrestrial body. This understanding can come from additional laboratory experiments under specific extraterrestrial conditions, as well as incorporating geomechanical modeling into interpretation of laboratory results and analysis of prior landing/sampling missions.

Planetary bodies — be they asteroids, comets, moons, or planets — are found at a wide variety of temperatures, pressures and saturations [52], and are composed of a vast array of materials both strong and weak. The temperatures explored in this study are

relevant to comets and asteroids throughout the solar system, where surface temperatures can reach below 90 K [70], and to planets and other celestial bodies with known cryogenic surface temperatures (Enceladus, Europa, Phobos and Deimos, the Moon, etc). This study observes the mechanical behavior of relatively weak saturated substrates under cryogenic temperatures and relatively low pressures.

However, previous studies [17] also involved similar experiments performed on significantly stronger granite samples (<1% porosity and a density of 2.64 g/cm^3). The composition of granite could be expected to be similar to that of a carbonaceous chondrite or any magmatic planetary body. The results of the study on the unconfined compressive strength of granites show a similar increase in the saturated strength at low temperatures, with a maximum occurring at 150 K; a result that is surprising given the low porosity nature of the granite. One would expect a low porosity to result in a low volume of water in the pores and therefore less of a strengthening effect. It seems, however, that the presence of water inside any pore space at sufficiently low temperature may increase the strength.

It is obvious that such an increase in strength as seen in this study will have profound effects on the energy required to drill into a saturated, frozen substrate. As mentioned, the specific energy of a material is the energy required to penetrate into it, and is a function of the material's compressive strength. A material such as a limestone, saturated and found at sufficiently low temperature, could have a compressive strength in excess of 200 MPa (Figure 3-1). Basalt, a more geologically reasonable asteroid analog, has a UCS in the range of 280 MPa and has been shown to have a specific energy (with rotary percussive drilling methods) of ~1000 MJ/m^3 [71].

If one assumes a frozen and saturated limestone to have a similar specific energy as basalt under the same drilling conditions, we can begin to look at drilling energy requirements. Current proposed extraterrestrial drills use 100 W of available power as a reasonable standard [4]. Assuming the required borehole has a radius of 0.01 m and a depth of 1 m, a specific energy of 1000 MJ/m^3 would result in a total required energy input of ~314 kJ and a total drilling time of ~52 min. This compares well to terrestrial testing of various substrates in a vacuum, in which the average drilling rate was 1 m/h with a 100 N weight on bit (WOB) [71].

The MUPUS-PEN, however, had 12 W of maximum available power and intended to penetrate into 2.6 x 10^{-5} m^3 of cometary material [72]. For a medium with a specific energy

of 1000 MJ/m^3, a total energy of 26 kJ is required and a total drilling time of 36 minutes. A material such as a tuff, on the other hand, if found saturated and at sufficiently low temperature, could have a compressive strength near to 100 MPa (assuming no confining stress). Though no data exists on the specific energy required to drill into such a material, Figure 3-6 suggests that it may be close to 700 MJ/m^3. Following the previous analysis, a total energy input of 18 kJ is expected with a total drilling time of 25 minutes. A very soft material (such as the unsaturated tuff with an unconfined compressive strength of less than 10 MPa) could have a specific energy of 20 MJ/m^3 or less, resulting in 260 J of total input and one minute of drilling time.

While there are sample retrieval missions currently proposed, the Rosetta/Philae mission in 2014 would have been the first to successfully retrieve a comet sample. Though the full details of Philae's scientific measurements on the comet 67P have yet to be analyzed and published, much of the data released to date indicates that the surface was far stronger than expected [9, 10, 11], and penetration by the sampling device (MUPUS-PEN) was not successful. Considering that cometary surfaces are thought to be mixtures of dust and water-ice, the results of this study indicate that significant strength should indeed be expected.

Philae, after being ejected from the Rosetta spacecraft, descended ballistically to the surface of 67P at its first landing site (Agilkia). Two subsystems — a cold gas system and anchoring harpoons — failed upon touchdown, leaving the lander to strike the surface at about 1 m/s relative to the comet surface. The impact bounced the lander off of the comet, and after about two hours of ballistic flight, multiple landings and subsequent bouncing, the lander came to rest at Abydos. The mechanical properties of the surface were estimated based on analysis of the lander mechanics [9].

Preliminary energy balance analysis from the initial touchdown at Agilkia shows that the comet surface is strongly damping, with roughly 50% to 80% of the lander's kinetic energy dissipated in the comet soil. However, the failure of the MUPUS-PEN probe to penetrate the surface at Abydos (even after three hours of hammering at increasing energy levels), indicates that the compressive strength of the surface material there is greater than 4 MPa. Additionally, the lander's feet and ice screws hardly penetrated the surface at all, which supports the hypothesis that the surface at Abydos is much harder than that at Agilkia. Current mechanical models suggest a compressive strength of 1 kPa at Agilkia and greater than 2 MPa at Abydos [9, 70].

Note, however, that these estimates are lower bounds based on the inability of the probe to penetrate the surface. The maximum energy level reached by the hammering mechanism was ~4 J [70], and recall the above estimate of 260 J required input energy to penetrate a 10 MPa material. This information, combined with the fact that the diurnal temperature of the comet varied between 90 K and 130 K, suggests that a much greater compressive strength is certainly possible.

The results of this study support such an assertion. If water is present in the pores of a cometary regolith, and the material is encountered at such low temperatures, our study implies that a significant compressive strength should be expected. At full saturation, compressive strengths in excess of several tens of MPa are plausible. Full saturation is not expected, and thus this estimate should be considered an upper bound, with the lower bound being that estimated by the MUPUS-PEN team (2 MPa). Future landers must be equipped with drills capable of providing greater than ~300 J of energy in order to penetrate a surface that could have a compressive strength of 10 MPa or greater.

An important note, however, is that the mechanism of ice deposition on comets, asteroids, and other planetary bodies is expected to be quite different than that on Earth. Namely, on airless and nearly-airless bodies, vapor-deposition is expected to be the primary deposition mechanism [74, 75, 76]. At low saturations, there is evidence showing that the microscopic structure of vapor-deposited ice is drastically different than that of conventional ice deposition [74, 77]. Ice can, depending on the pressure and temperature conditions, deposit either at grain contacts or at surface defects within a granular material (Figure 4-1).

Ice that deposits at grain contacts is known as "necking" ice. This results in ice structures very similar to those created on Earth by saturation of a granular material with water prior to freezing (the water will coat the grains and freeze in place).

However, under certain conditions [74, 77], ice will deposit at surface defects and grow filaments in the direction of an external thermal gradient. The resulting ice structure, known as "filament" ice, is unlike any ice structure that would form under typical laboratory saturation techniques (as performed in this study and others [78]). The nature of the filaments suggests that this could be a weaker structure within the granular material than necking ice.

Furthermore, while 5 MPa of confining pressure used in the experiments to reduce data scatter, it is unlikely that such pressures would be encountered in the near-surface of a

nearly-airless or airless body. With no surface pressure, most of these bodies would have to be exceptionally large (planet-size) in order to have subsurface pressures that reach 5 MPa. For example, the subsurface pressure of Ceres would reach 5 MPa at about 8500 m depth, as calculated using the standard equation for overburden pressure:

$$p(z) = p_o + g \int_0^z \rho(z) dz \tag{4.1}$$

where p_o is the surface pressure in Pa (assumed to be zero for airless bodies), g is the gravitational acceleration of the body (roughly 0.284 m/s^2), ρ is the average body density (2.08 g/cm^3 for Ceres, and assumed to be constant with depth), and z is depth in m. A smaller (airless) body would not be expected to reach 5 MPa at any depth.

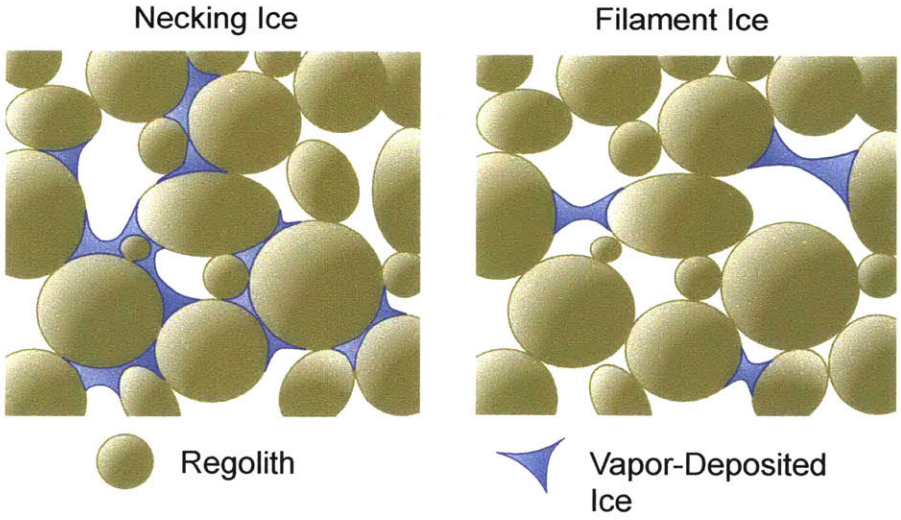

Figure 4-1: Schematic representation of "necking" and "filament" ice as observed by Hudson [74] and Siegler [77]. Due to the structure of filament ice, it is speculated to be mechanically weaker than the structure formed by necking.

Therefore, the values of compressive strength determined in this study (saturated under normal laboratory conditions and 5 MPa confining pressure), should be recognized as a potential upper bound to the strength expected on asteroid or comet near-surfaces.

With multiple sample-retrieval missions planned for the near future and an intent to make in situ resource utilization a reality, the increase in compressive strength of a saturated, porous material is a critical consideration in ensuring mission success. Expecting and preparing for very hard surfaces with a strength greater than 10 to 50 MPa will help our

future explorers access the subsurface of pristine celestial bodies and return the samples to Earth for analysis.

The results of this study also show that more research needs to be done in order to fully explore the variety of materials, saturations, pressures, and temperatures that we are likely to encounter in our solar system and beyond. In particular, knowledge of the mechanical properties is severely lacking. Additional experiments exploring the behavior observed in this study at the extremes of temperature and pressure will serve to expand our knowledge and prepare us for the future extraterrestrial scientific endeavors we aim to undertake.

Appendix A

Stress and Strain Corrections

Multiple corrections need to be made to the recorded data in order to provide an accurate estimation of the stress imparted on, and the strain undergone by, the sample.

Stress corrections are relatively simple, and involve zeroing the load reading at the point of first contact (FC), then converting from millivolts to MPa using an established conversion factor:

$$\sigma_d = (L - L_o)c_s \tag{A.1}$$

where σ_d is the differential stress (axial stress minus confining stress), L and L_o are the measured load and the load reading at first contact, respectively, and c_s is a the apparatus conversion factor from mV to MPa.

Converting piston displacement to sample strain is a slightly more complex process. The piston is not completely rigid and undergoes a small amount of strain proportional to the load applied (u_{el}). The recorded displacement of the piston (u_{rec}) is the difference between the measured displacement (d) and the zero point occurring at the first contact position (d_o). That is,

$$u_{rec} = d - d_o \tag{A.2}$$

$$u_{el} = \sigma_d c_{el} \tag{A.3}$$

where c_{el} is the conversion factor from inches displacement to MPa.

A correction must be applied to the displacement that takes into account the furthest advancement of the piston (u_{ref_f}), the maximum displacement experienced by the piston due to the stress imparted on the sample (u_{el_f}), and the actual shortening of the sample as

measured post-experiment (u_{act_f}):

$$u_{corr} = \frac{u_{act_f}}{u_{rec_f} - u_{el_f}} \tag{A.4}$$

The actual displacement is therefore

$$u_{act} = (u_{rec} - u_{el})u_{corr} \tag{A.5}$$

and the resulting strain is

$$\epsilon = \frac{u_{act}}{l_o} \tag{A.6}$$

where l_o is the original sample length.

Appendix B

Indiana Limestone Tests

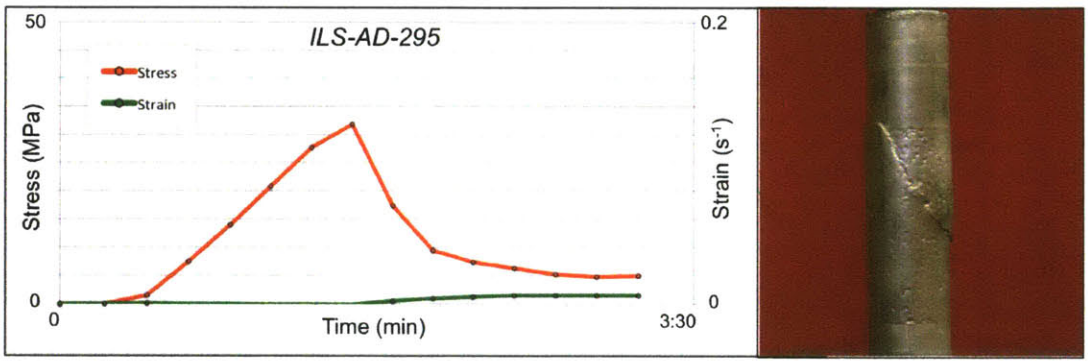

Figure B-1: Stress-strain profile and deformation of sample ILS-AD-295.

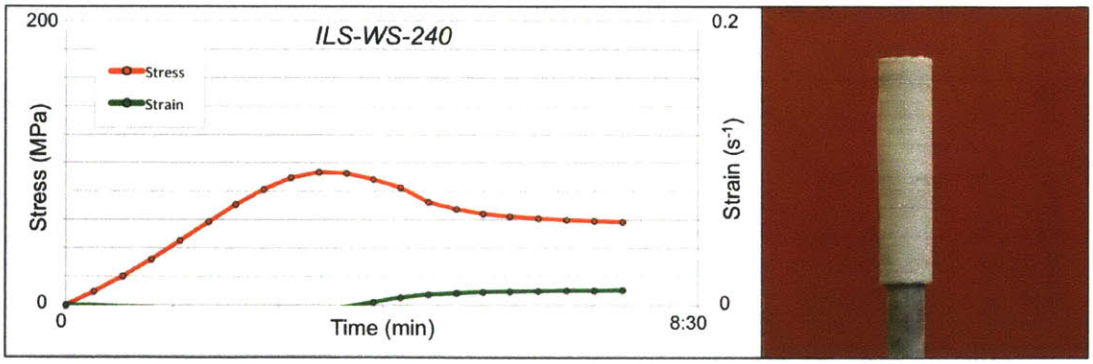

Figure B-2: Stress-strain profile and deformation of sample ILS-WS-240.

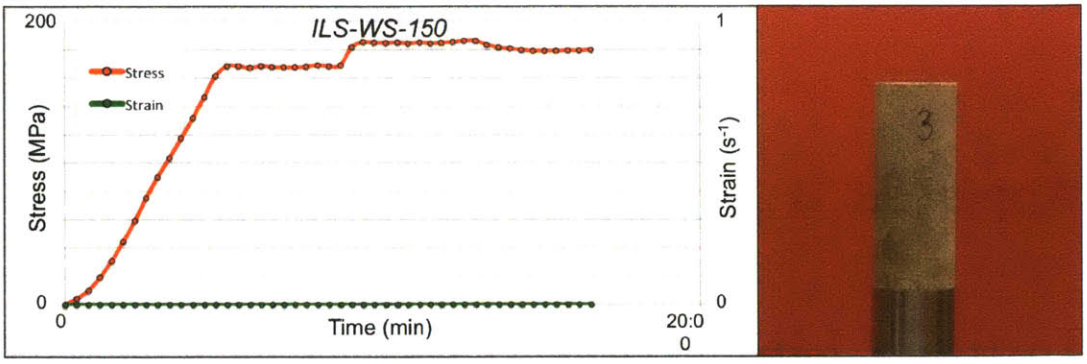

Figure B-3: Stress-strain profile and deformation of sample ILS-WS-150.

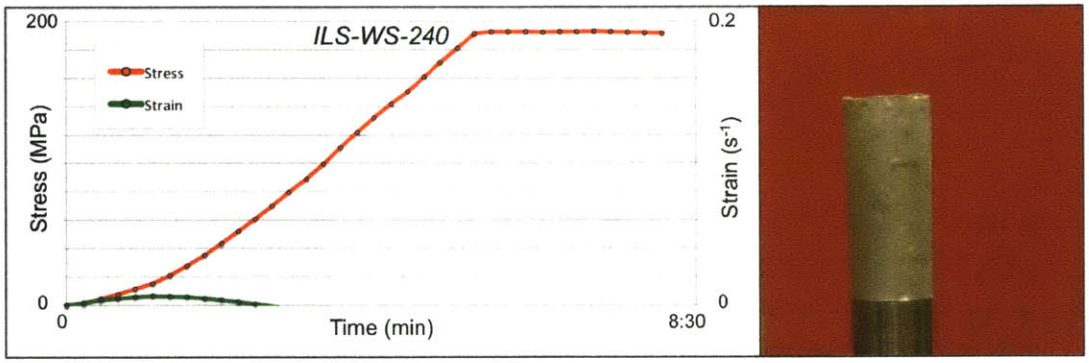

Figure B-4: Stress-strain profile and deformation of sample ILS-WS-77.

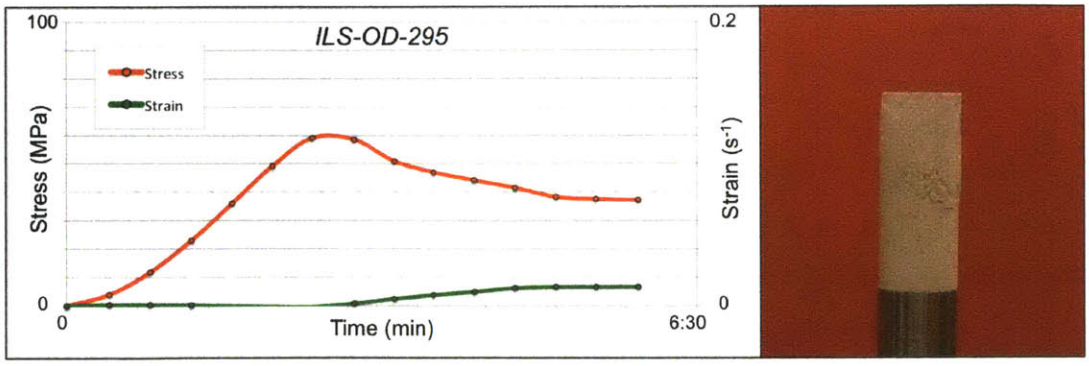

Figure B-5: Stress-strain profile and deformation of sample ILS-OD-295.

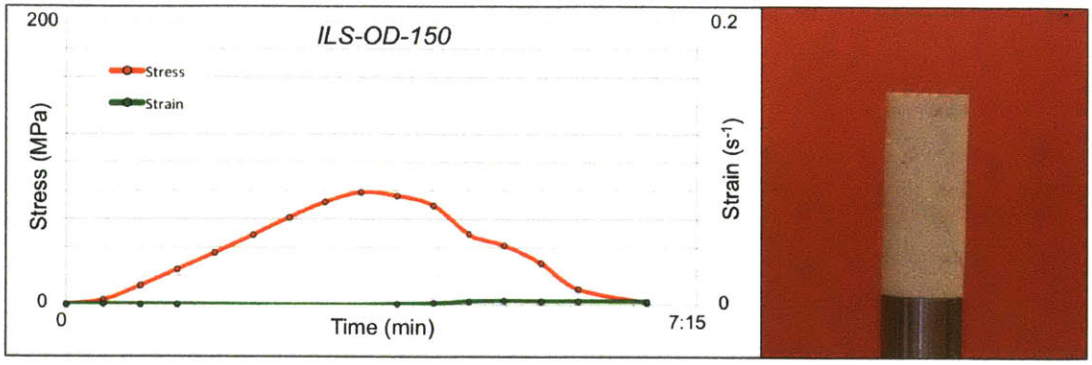

Figure B-6: Stress-strain profile and deformation of sample ILS-OD-150.

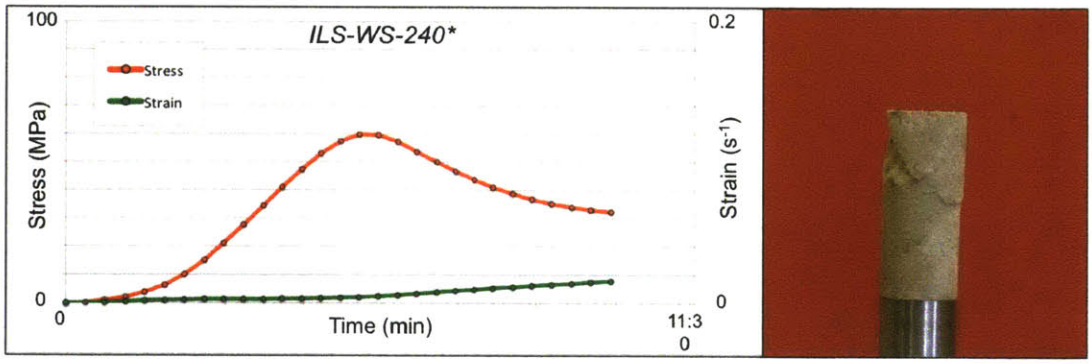

Figure B-7: Stress-strain profile and deformation of sample ILS-WS-240* (reloaded ILS-WS-240).

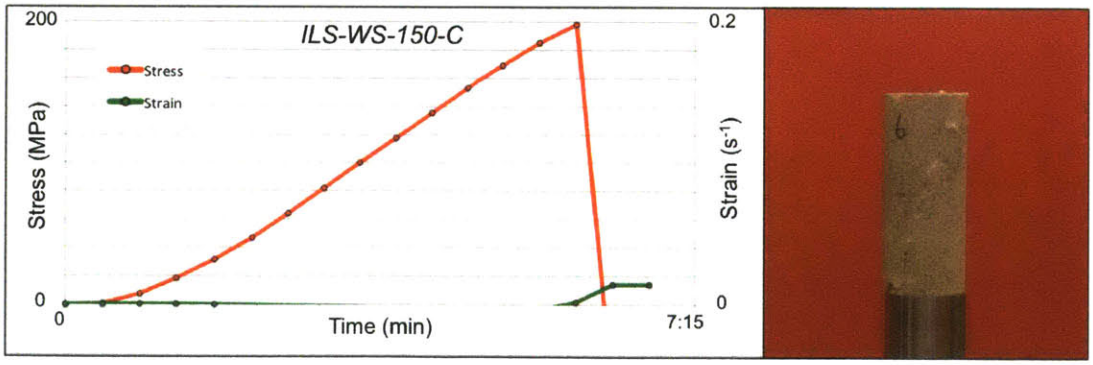

Figure B-8: Stress-strain profile and deformation of sample ILS-WS-150-C (thermally cycled ILS-WS-150).

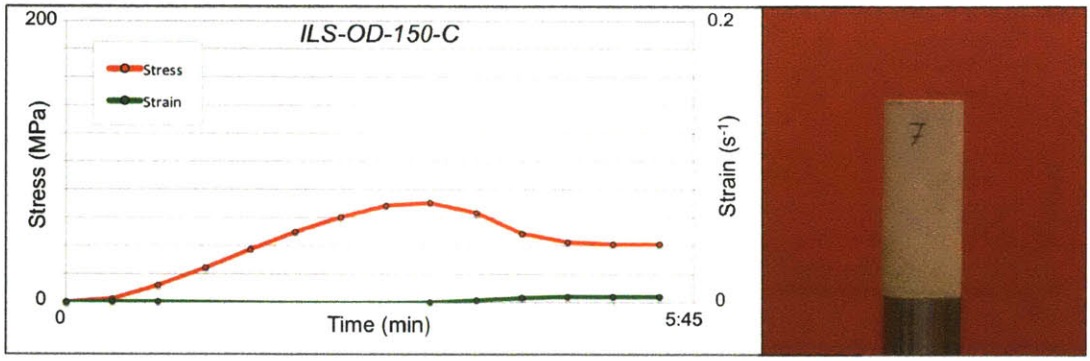

Figure B-9: Stress-strain profile and deformation of sample ILS-OD-150-C (thermally cycled ILS-OD-150).

Appendix C

Bishop Tuff Tests

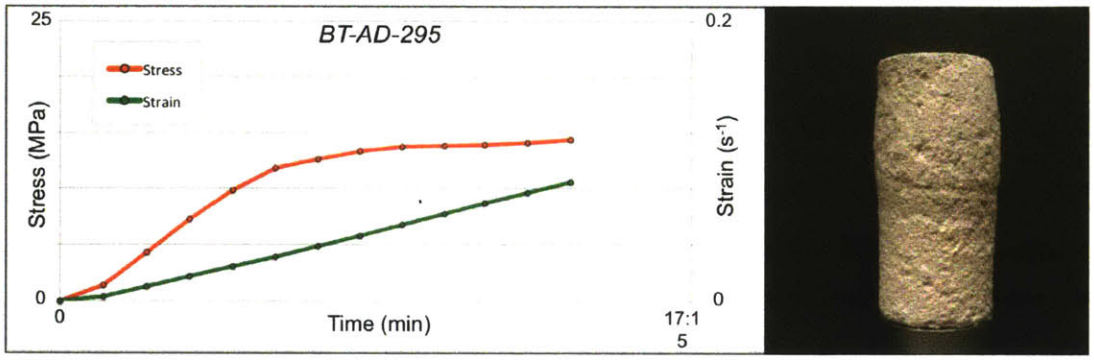

Figure C-1: Stress-strain profile and deformation of sample BT-AD-295.

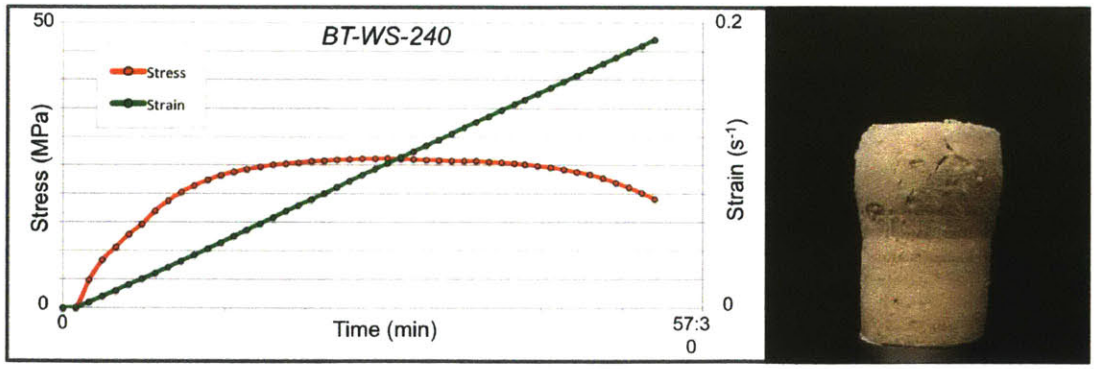

Figure C-2: Stress-strain profile and deformation of sample BT-WS-240.

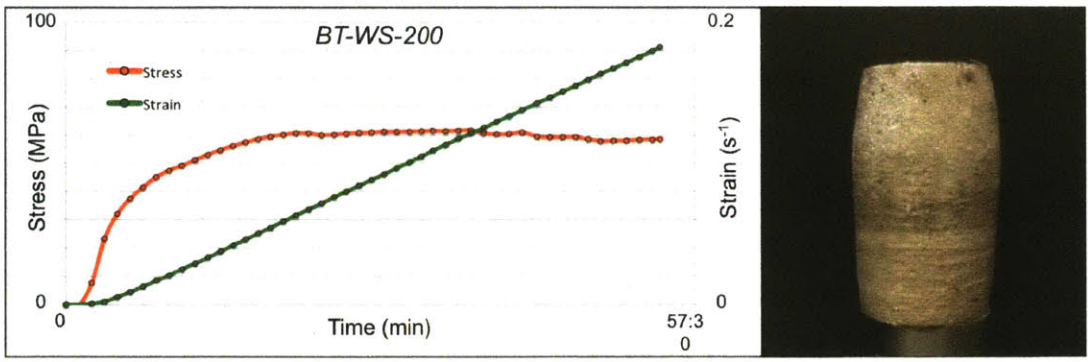

Figure C-3: Stress-strain profile and deformation of sample BT-WS-200.

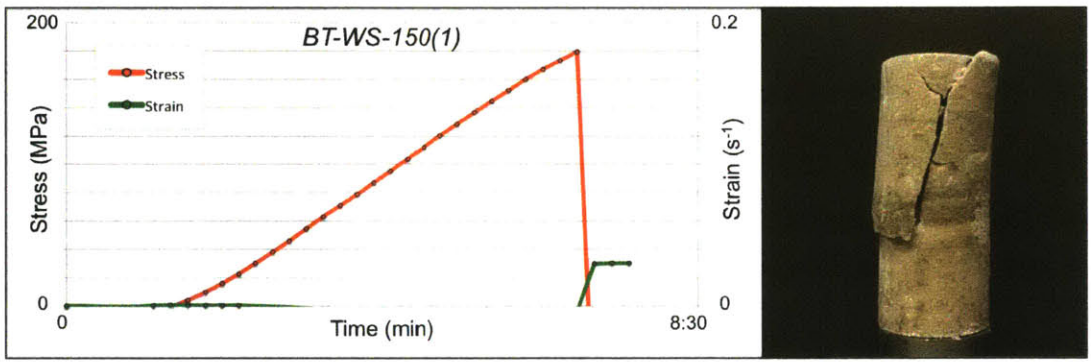

Figure C-4: Stress-strain profile and deformation of sample BT-WS-150(1).

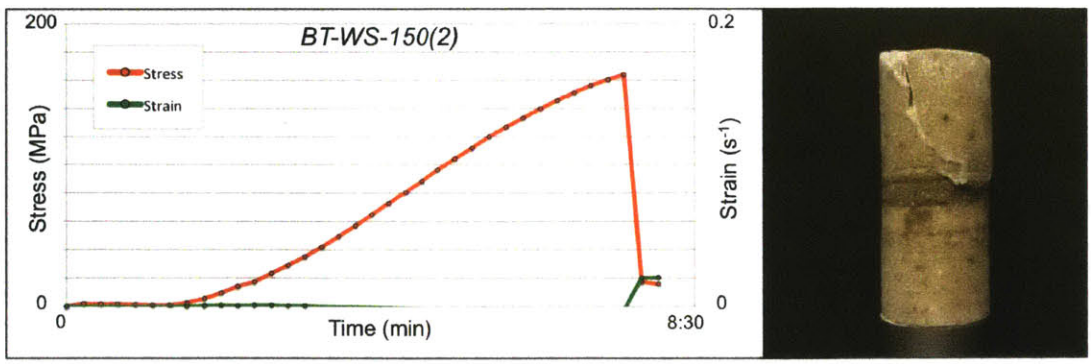

Figure C-5: Stress-strain profile and deformation of sample BT-WS-150(2).

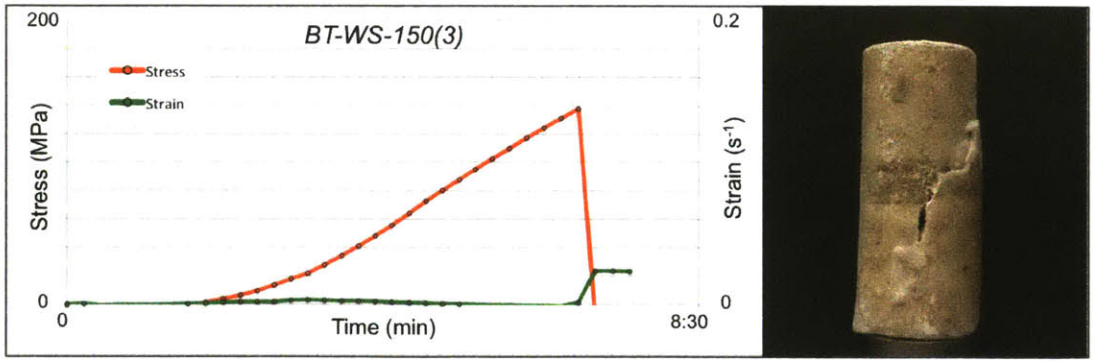

Figure C-6: Stress-strain profile and deformation of sample BT-WS-150(3).

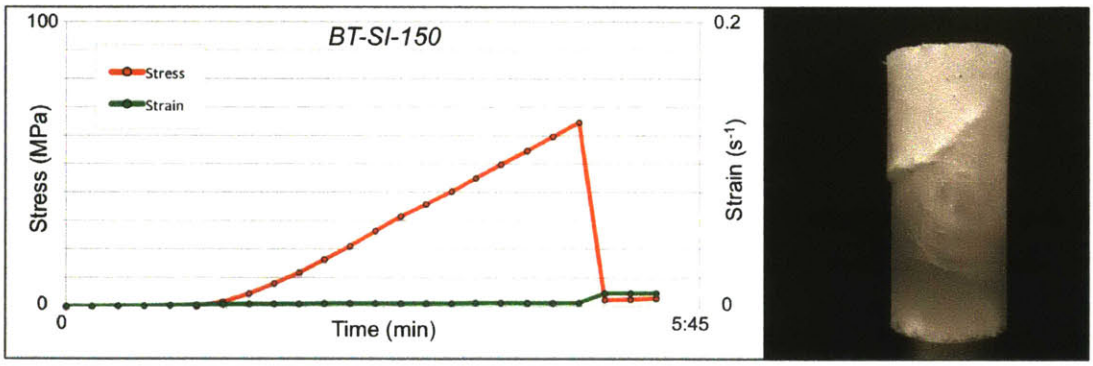

Figure C-7: Stress-strain profile and deformation of standard ice sample BT-SI-150.

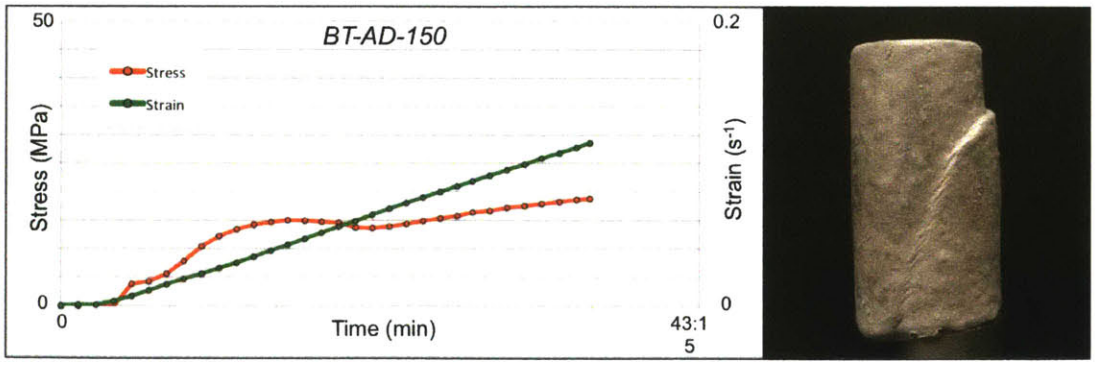

Figure C-8: Stress-strain profile and deformation of sample BT-AD-150.

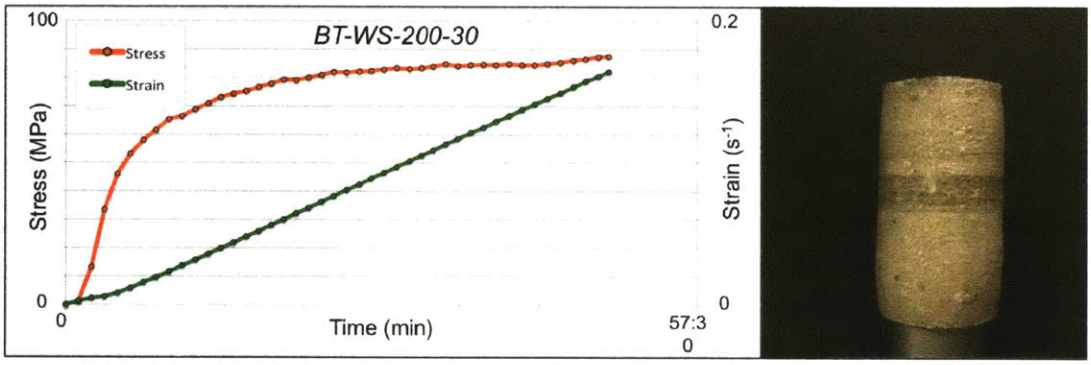

Figure C-9: Stress-strain profile and deformation of sample BT-WS-200-30.

Bibliography

[1] National Research Council. Vision and Voyages for Planetary Science in the Decade 2013-2022. Technical report, 2013.

[2] V. Badescu. *Asteroids: Prospective Energy and Material Resources.* 2013.

[3] T. Simon and K. Sacksteder. NASA In-Situ Resource Utilization (ISRU) Development & Incorporation Plans. In *Technology Exchange Conference*, Galveston, TX., 2007.

[4] K. A. Zacny, Y. Bar-Cohen, and M. Brennan. Drilling systems for extraterrestrial subsurface exploration. *Astrobiology*, 8(3):665–706, 2008.

[5] G. J. Consolmagno. Ice-rich moons and the physical properties of ice. *The Journal of Physical Chemistry*, 285(1982):4204–4208, 1983.

[6] German Aerospace Center (DLR). Churyumov-Gerasimenko âĂŞ hard ice and organic molecules, 2014.

[7] Japan Aerospace Exploration Agency. JAXA Asteroid Explorer "Hayabusa2", 2014.

[8] R. P. Binzel. Find asteroids to get to Mars. *Nature*, 514:559–561, 2014.

[9] J. Biele, S. Ulamec, M. Maibaum, R. Roll, L. Witte, E. Jurado, P. Muñoz, W. Arnold, H. Auster, C. Casas, C. Faber, C. Fantinati, F. Finke, H. Fischer, K. Geurts, C. Güttler, P. Heinisch, A. Herique, S. Hviid, G. Kargl, M. Knapmeyer, J. Knollenberg, W. Kofman, N. Kömle, E. Kührt, V. Lommatsch, S. Mottola, R. Pardo de Santayana, E. Remetean, F. Scholten, K. J. Seidensticker, H. Sierks, and T. Spohn. The landing(s) of Philae and inferences about comet surface mechanical properties. *Science (New York, N.Y.)*, 349(6247):aaa9816, 2015.

[10] European Space Agency. Three touchdowns for Rosetta's lander, 2014.

[11] E. Hand. Philae probe makes bumpy touchdown on a comet. *Science*, 346(6212):900–901, 2014.

[12] C. P. McKay, C. R. Stoker, B. J. Glass, A. I. Dave, A. F. Davila, J. L. Heldmann, M. M. Marinova, A. G. Fairen, R. C. Quinn, K. A. Zacny, G. Paulsen, P. H. Smith, V. Parro, D. T. Andersen, M. H. Hecht, D. Lacelle, and W. H. Pollard. The Icebreaker Life Mission to Mars: A Search for Biomolecular Evidence for Life. *Astrobiology*, 13(4):334–354, apr 2013.

[13] K. A. Zacny, J. Craft, M. Hedlund, J. Wilson, P. Chu, P. Fink, R. Mueller, G. Galloway, and G. Mungas. Novel Approaches to Drilling and Excavation on the Moon. In *AIAA SPACE Conference*, number September, pages 1–12, Pasadena, CA, 2009.

[14] Jet Propulsion Laboratory. Vesta Likely Cold and Dark Enough for Ice, 2012.

[15] R. W. Heins and T. O. Friz. The Effect of Low Temperature on Some Physical Properties of Rocks. *SPE*, 1967.

[16] A. S. Kurilko and M. D. Novopashin. Features of Low Temperature Effect Upon Strength of Enclosing Rock and Kimberlite in the "Udachnaya" Pipe. *Journal of Mining Science*, 41(2):119–122, 2005.

[17] M. Mellor. Strength and Deformability of Rocks at Low Temperatures. Technical report, Cold Regions Research and Engineering Laboratory, Hanover, NH, 1971.

[18] E. R. Podnieks, P. G. Chamberlain, and R. E. Thill. Environmental Effects on Rock Properties. In K. E. Gray, editor, *Basic and Applied Rock Mechanics*, chapter 8, pages 215–241. 1968.

[19] H. C. Heard, W. B. Durham, C. O. Boro, and S. H. Kirby. A Triaxial Deformation Apparatus for Service at $77 < T < 273$ K. *Geophysical Monograph Series*, 56:225–228, 1990.

[20] D. C. Richardson, Z. M. Leinhardt, H. J. Melosh, W. F. Bottke Jr, and E. Asphaug. Gravitational aggregates: Evidence and evolution. In *Asteroids III*, pages 501–515. University of Arizona Press, 2002.

[21] A. S. Rivkin and J. P. Emery. Detection of ice and organics on an asteroidal surface. *Nature*, 464(7293):1322–1323, 2010.

[22] F. Raulin, C. Mckay, J. Lunine, and T. Owen. Titan's Astrobiology. In *Titan from Cassini-Huygens*, chapter 9, pages 215–233. Springer Berlin Heidelberg, 2009.

[23] W. C. Feldman, S. Maurice, D. J. Lawrence, R. C. Little, S. L. Lawson, O. Gasnault, R. C. Wiens, B. L. Barraclough, R. C. Elphic, T. H. Prettyman, J. T. Steinberg, and A. B. Binder. Evidence for water ice near the lunar poles. *Journal of Geophysical Research*, 106(E10):23231, 2001.

[24] D. J. Lawrence, W. C. Feldman, J. O. Goldsten, S. Maurice, P. N. Peplowski, B. J. Anderson, D. Bazell, R. L. McNutt, L. R. Nittler, T. H. Prettyman, D. J. Rodgers, S. C. Solomon, and S. Z. Weider. Evidence for water ice near Mercury's north pole from MESSENGER Neutron Spectrometer measurements. *Science*, 339(January):292–6, 2013.

[25] T. H. Prettyman, W. C. Feldman, F. P. Ameduri, B. L. Barraclough, E. W. Cascio, K. R. Fuller, H. O. Funsten, D. J. Lawrence, G. W. McKinney, C. T. Russell, S. A. Soldner, S. A. Storms, C. Szeles, and R. L. Tokar. Gamma Ray and Neutron Spectrometer for the Dawn Mission to 1 Ceres and 4 Vesta. *IEEE Transactions on Nuclear Science*, 50(4):1190–1197, 2003.

[26] E. M. Palmer, E. Heggy, M. T. Capria, F. Tosi, and C. T. Russell. Dielectric Properties of the Surface of Asteroid Vesta from Dawn VIR Thermal Observations. *44th Lunar and Planetary Science Conference*, 2013.

[27] E. Heggy, E. M. Palmer, W. Kofman, S. M. Clifford, K. Righter, and A. Hérique. Radar properties of comets: Parametric dielectric modeling of Comet 67P/Churyumov-Gerasimenkol. Heggy, E. et al. Radar properties of comets: Parametric dielectric modeling of Comet 67P/Churyumov-Gerasimenko. Icarus 221, 925âĂŞ939 (2012). *Icarus*, 221(2):925–939, 2012.

[28] L. M. Prockter. Ice in the solar system. *Johns Hopkins APL Technical Digest*, 26(2):175–188, 2005.

[29] N. Schorghofer. The Lifetime of Ice on Main Belt Asteroids. *The Astrophysical Journal*, 682(1):697–705, 2008.

[30] E. M. Schulson. The Structure and Mechanical Behavior of Ice. *The Journal of The Minerals, Metals & Materials Society (TMS)*, 51(2):21–27, 1999.

[31] N. Anderson. The Many Phases of Ice, 2009.

[32] W. B. Durham, S. H. Kirby, and L. A. Stern. Creep of water ices at planetary conditions: A compilation. *Journal of Geophysical Research*, 102(E7):16,293–16,302, 1997.

[33] W. B. Durham, O. Prieto-Ballesteros, D. L. Goldsby, and J. S. Kargel. Rheological and thermal properties of icy materials. *Space Science Reviews*, 153(1-4):273–298, 2010.

[34] J. Seki and H. Hasegawa. The heterogeneous condensation of interstellar ice grains. *Astrophysics and Space Science*, 94(1):177–189, 1983.

[35] A. Kouchi, T. Yamamoto, T. Kozasa, T. Kuroda, and J. M. Greenberg. Conditions for condensation and preservation of amorphous ice and crystallinity of astrophysical ices. *Astronomy and Astrophysics*, (290):1009 – 1018, 1994.

[36] M. H. Moore and R. L. Hudson. Far-infrared spectral studies of phase changes in water ice induced by proton irradiation. *Astrophysical Journal*, 401(1):353 – 360, 1992.

[37] C. C.. Porco, P Helfenstein, P. C. Thomas, A. P. Ingersoll, J. Wisdom, R West, G Neukum, T. Denk, R. Wagner, T. Roatsch, S. Kieffer, E. Turtle, A. McEwen, T. V. Johnson, J. Rathbun, J. Veverka, D. Wilson, J. Perry, J Spitale, A. Brahic, J. A. Burns, A. D. Delgenio, L. Dones, C. D. Murray, and S. Squyres. Cassini observes the active south pole of Enceladus. *Science*, 311(5766):1393–1401, 2006.

[38] A. S. Rivkin. NEO/Phobos/Deimos Strategic Knowledge Gaps Special Action Team Final Report. Technical report, Small Bodies Assessment Group, 2012.

[39] M. Delbo, M. Mueller, J. P. Emery, B. Rozitis, and M. T. Capria. Asteroid thermophysical modeling. *Asteroids IV*, 2015.

[40] F. P. Fanale and J. R. Salvail. The water regime of asteroid (1) Ceres. *International Journal of Solar System Studies*, 82:97–110, 1989.

[41] F. P. Fanale and J. R. Salvail. Evolution of the water regime of Phobos. *Icarus*, 88(2):380–395, 1990.

[42] D. Prialnik and E. D. Rosenberg. Can ice survive in main-belt comets? Long-term evolution models of comet 133P/Elst-Pizarro. *Monthly Notices of the Royal Astronomical Society: Letters*, 399(1):L79–L83, 2009.

[43] N. Schorghofer. Predictions of Depth to Ice on Asteroid Ceres. In *46th Lunar and Planetary Science Conference*, 2015.

[44] D. T. Britt, D. Yeomans, K. Housen, and G. J. Consolmagno. Asteroid density, porosity, and structure. In *Asteroids III*, pages 485–500. University of Arizona Press, 1987.

[45] B. Evans, J. T. Fredrich, and T. Wong. The brittle-ductile transition in rocks: Recent experimental and theoretical progress. *Geophysical Monograph*, 56:1–20, 1990.

[46] M. S. Paterson and T. Wong. *Experimental Rock Deformation - The Brittle Field.* Springer-Verlag, second edition, 2005.

[47] H. Horii and S. Nemat-Nasser. Compression-induced microcrack growth in brittle solids: Axial splitting and shear failure. *Journal of Geophysical Research*, 90(B4):3105, 1985.

[48] H. Horii and S. Nemat-Nasser. Brittle Failure in Compression: Splitting, Faulting and Brittle-Ductile Transition. *Philosophical Transactions of the Royal Society A: Mathematical, Physical and Engineering Sciences*, 319(1549):337–374, 1986.

[49] W. B. Durham, H. C. Heard, and S. H. Kirby. Experimental Deformation of Polycrystalline H2O Ice at High Pressure and Low Temperature - Preliminary Results. In *Proceedings of the Fourteenth Lunar and Planetary Science Conference, Part 1*, volume 88, pages B377–B392, 1983.

[50] S. H. Kirby, W. B. Durham, M. L. Beeman, H. C. Heard, and M. A. Daley. Inelastic Properties of Ice 1h at Low Temperatures and High Pressures. *Journal de Physique*, C1(3):227–232, 1987.

[51] J. Weiss and E. M. Schulson. The failure of fresh-water granular ice under multiaxial compressive loading. *Acta Metallurgica et Materialia*, 43(6):2303–2315, 1995.

[52] M. L. Nelson, D. T. Britt, and L. A. Lebofsky. Review of Asteroid Compositions. In *Resources of near-Earth space*, pages 493–522. University of Arizona Press, 1993.

[53] A. S. Rivkin, E. S. Howell, F. Vilas, and L. A. Lebofsky. Hydrated Minerals on Asteroids: The Astronomical Record. In *Asteroids III*, pages 235 – 253. University of Arizona Press, 2002.

[54] G. J. Flynn, L. B. Moore, and W. Klöck. Density and porosity of stone meteorites: Implications for the density, porosity, cratering, and collisional disruption of asteroids. *Icarus*, 142(1):97–105, 1999.

[55] B. Amadei, V. Janoo, M. Robison, and R. Kuberan. Strength of Indiana limestone in true biaxial loading conditions. In *The 25th US Symposium on Rock Mechanics*, pages 338–348, 1984.

[56] C. J. N. Wilson and W. Hildreth. The Bishop Tuff: New insights from eruptive stratigraphy. *The Journal of Geology*, 105(4):407–440, 1997.

[57] G.A. Izett, J.D. Obradovich, and H.H. Mehnert. The Bishop Ash Bed (Middle Pleistocene) and Some Older (Pliocene and Pleistocene) Chemically and Mineralogically Similar Ash Beds in California, Nevada, and Utah. *U.S. Geological Society Bulletin 1675*, 1988.

[58] A. E. Rubin. Mineralogy of meteorite groups. *Meteoritics & Planetary Science*, 32(2):231–247, 1997.

[59] M. S. Hanner and J. P. Bradley. Composition And Mineralogy Of Cometary Dust. In *Comets II*, pages 555–564. 2004.

[60] J. P. Evans and K. K. Bradbury. Faulting and Fracturing of Nonwelded Bishop Tuff, Eastern California. *Vadose Zone Journal*, 3(2):602, 2004.

[61] E. Orowan. The Fatigue of Glass Under Stress. *Nature*, 154:341–343, 1944.

[62] C. Gurney. Delayed fracture in glass. *Proceedings of the Physical Society*, 59:169–185, 2002.

[63] R. Teale. The Concept of Specific Energy in Rock Drilling. *International Journal of Rock Mechanics and Mining Science*, 2(1):57–73, 1965.

[64] C.A. Coulomb. *Essai sur une application des reÌĂgles de maximis & minimis aÌĂ quelques probleÌĂmes de statique, relatifs aÌĂ l'architecture.* De l'Imprimerie Royale, Paris, 1776.

[65] J. Ondrasina, D. Kirchner, and S. Siegesmund. Freeze-thaw cycles and their influence on marble deterioration: a long-term experiment. *Geological Society, London, Special Publications*, 205:9–18, 2002.

[66] W. B. Durham, S. H. Kirby, and L. A. Stern. Effects of Dispersed Particulates on the Rheology of Water Ice at Planetary Conditions. *Journal of Geophysical Research*, 97(E12):20,883–20,897, 1992.

[67] M. Horanyi. NASA SSERVI-IMPACT. Technical report, LASP, University of Colorado, Boulder, CO, 2014.

[68] H. Viles, B. Ehlmann, C. F. Wilson, T. Cebula, M. Page, and M. Bourke. Simulating weathering of basalt on Mars and Earth by thermal cycling. *Geophysical Research Letters*, 37(18):1–5, 2010.

[69] S. Ulamec and J. Biele. Surface elements and landing strategies for small bodies missions - Philae and beyond. *Advances in Space Research*, 44(7):847–858, 2009.

[70] T. Spohn, J. Knollenberg, A. J. Ball, M. Banaszkiewicz, J. Benkhoff, M. Grott, J. Grygorczuk, C. Huttig, A. Hagermann, G. Kargl, E. Kaufmann, N. Komle, E. Kuhrt, K. J. Kossacki, W. Marczewski, I. Pelivan, R. Schrodter, and K. Seiferlin. Thermal and mechanical properties of the near-surface layers of comet 67P/Churyumov-Gerasimenko. *Science*, 349(6247):aab0464–aab0464, 2015.

[71] K. A. Zacny and G. A. Cooper. Coring basalt under Mars low pressure conditions. *Mars*, 3:1–11, 2007.

[72] German Aerospace Agency (DLR). Philae Lander Facts Sheet.

[73] J. Grygorczuk, M. Banaszkiewicz, K. Seweryn, and T. Spohn. MUPUS insertion device for the Rosetta mission. *Journal of Telecomunications and Information Technology*, (January):50–53, 2007.

[74] T. L. Hudson. *Growth, Diffusion, and Loss of Subsurface Ice on Mars: Experiments and Models.* PhD thesis, California Institute of Technology, 2008.

[75] B. M. Jakosky, A. P. Zent, and R. W. Zurek. The Mars Water Cycle: Determining the Role of Exchange with the Regolith. *Icarus*, 130(1):87–95, 1997.

[76] N. Schorghofer and O. Aharonson. Stability and exchange of subsurface ice on Mars. *Journal of Geophysical Research*, 110, 2005.

[77] M. Siegler, O. Aharonson, E. Carey, M. Choukroun, T. L. Hudson, N. Schorghofer, and S. Xu. Measurements of thermal properties of icy Mars regolith analogs. *Journal of Geophysical Research E: Planets*, 117(3):1–24, 2012.

[78] J. E. Kleinhenz and D. Linne. Preparation of a Frozen Regolith Simulant Bed for ISRU Component Testing in a Vacuum Chamber. In *51st AIAA Aerospace Sciences Meeting including the New Horizons Forum and Aerospace Exposition*, number January. Aerospace Sciences Meetings, 2013.